Brain exposure to SARS-CoV-2 virions perturbs synaptic homeostasis

Emma Partiot, Aurélie Hirschler, Sophie Colomb, Willy Lutz, Tine Claeys, François Delalande, Maika S Deffieu, Yonis Bare, Judith Rebecca Elise Roels, Barbara Gorda, et al.

To cite this version:

Emma Partiot, Aurélie Hirschler, Sophie Colomb, Willy Lutz, Tine Claeys, et al.. Brain exposure to SARS-CoV-2 virions perturbs synaptic homeostasis. Nature Microbiology, 2024, 9 (5), pp.1189-1206. 10.1038/s41564-024-01657-2 . hal-04532958

HAL Id: hal-04532958
https://hal.science/hal-04532958v1

nature microbiology

Article

https://doi.org/10.1038/s41564-024-01657-2

Brain exposure to SARS-CoV-2 virions perturbs synaptic homeostasis

Received: 6 April 2023

Accepted: 4 March 2024

Emma Partiot[1,2], Aurélie Hirschler[3,4], Sophie Colomb[5,6], Willy Lutz[1,2,7], Tine Claeys[8,9], François Delalande[3,4], Maika S. Deffieu[1,2], Yonis Bare[1,2], Judith R. E. Roels[10], Barbara Gorda[1,2], Joanna Bons[3,4], Domitille Callon[11,12], Laurent Andreoletti[11,12], Marc Labrousse[12,13], Frank M. J. Jacobs[10], Valérie Rigau[2,14], Benoit Charlot[2,15], Lennart Martens[8,9], Christine Carapito[3,4], Gowrishankar Ganesh[2,7] & Raphael Gaudin[1,2]

Severe acute respiratory syndrome coronavirus 2 (SARS-CoV-2) infection is associated with short- and long-term neurological complications. The variety of symptoms makes it difficult to unravel molecular mechanisms underlying neurological sequalae after coronavirus disease 2019 (COVID-19). Here we show that SARS-CoV-2 triggers the up-regulation of synaptic components and perturbs local electrical field potential. Using cerebral organoids, organotypic culture of human brain explants from individuals without COVID-19 and post-mortem brain samples from individuals with COVID-19, we find that neural cells are permissive to SARS-CoV-2 to a low extent. SARS-CoV-2 induces aberrant presynaptic morphology and increases expression of the synaptic components Bassoon, latrophilin-3 (LPHN3) and fibronectin leucine-rich transmembrane protein-3 (FLRT3). Furthermore, we find that LPHN3-agonist treatment with Stachel partially restored organoid electrical activity and reverted SARS-CoV-2-induced aberrant presynaptic morphology. Finally, we observe accumulation of relatively static virions at LPHN3–FLRT3 synapses, suggesting that local hindrance can contribute to synaptic perturbations. Together, our study provides molecular insights into SARS-CoV-2–brain interactions, which may contribute to COVID-19-related neurological disorders.

The coronavirus disease 2019 (COVID-19) results from the severe acute respiratory syndrome coronavirus 2 (SARS-CoV-2), which has caused an unprecedented pandemic. The most recognized organ to be impacted by the infection is the lower respiratory tract, but an increasing number of studies indicate that the infection has also wide consequences on the central nervous system (CNS)[1]. Patients with COVID-19 exhibit a large range of neurological, cognitive and psychiatric disorders[2–7], and altered mental status has been widely reported as a long-term symptom of neuroCOVID, including psychotic disorder, cognitive deficit, dementia and epilepsy or seizures[8–14]. COVID-associated neurocognitive disorders (CAND) cannot solely be attributed to the anxiogenic period (because the consequences of COVID-19 were not well known at the time), as non-hospitalized patients with COVID-19 showed significantly more psychiatric disorders compared to flu-infected patients (patients who were also sick during the same period)[10].

The long-term neurological impairments may be explained in part by several non-exclusive mechanisms, including neuroinflammation, autoimmunity, microvascular-related disease, reactivation of latent herpesvirus and hypoxia[15], but it remains to be established whether SARS-CoV-2 could play a more direct role in CAND in the case

A full list of affiliations appears at the end of the paper. e-mail: raphael.gaudin@irim.cnrs.fr

of apparently 'asymptomatic' patients. Indeed, SARS-CoV-2-infected cells were found in the brain of patients who died up to several months following COVID-19 infection, suggesting that the CNS could represent a reservoir for the virus, where low-level replication can occur[16]. Yet, the direct impact of the exposure of the brain to SARS-CoV-2 remains unknown. The heterogeneity of the models used in neuroCOVID studies and their limitations[17–20] have been hampering the discovery of molecular and subcellular events from which the neural perturbations originate. Given the wide variety of neurological symptoms frequently described for patients with asymptomatic/mild COVID-19[21], further in-depth investigations on how virus–host interactions participate in SARS-CoV-2-induced neural circuit dysfunction and cognitive impairment are required.

Patients with COVID-19 who are asymptomatic or with mild symptoms can exhibit persistently abnormal electroencephalograms (EEGs)[22–24], indicating that subtle impairments in electric signal transmission occur. Such signals propagate in the brain through inter-neuronal synapses, and SARS-CoV-2 has previously been shown to impact the expression levels of synaptic components[25,26]. However, while a study identified a down-regulation of synaptic vesicle component messenger RNAs[25], another one highlighted that SARS-CoV-2 infection led to overexpression of genes related to synapse assembly, synaptic transmission and post-synaptic membrane potential specifically, all particularly in neurons[26]. This latter study revealed that SARS-CoV-2 infection of cortical organoids leads to microglia-dependent pruning of defective synapses. Hence, an equilibrium may exist between SARS-CoV-2-induced dysfunctional synapse accumulation and microglia-mediated synaptic pruning, but the molecular mechanisms governing this fine-tuned balance is unknown.

In this Article, we showed that SARS-CoV-2 infection of cerebral organoids devoid of microglial cells induces an up-regulation of the expression of synaptic components, associated to enlarged presynaptic structures. Interestingly, the supplementation of cerebral organoids with infiltrated monocytes which may show microglial features reverted this phenotype, suggesting that it turned the balance in favour of monocytic/microglial pruning of synapses, as previously proposed[26]. Because organoids resemble embryonic and not adult brain structure, we also used organotypic culture of post-mortem adult human cortical brain explants (OPAB)[27], and we highlighted in this model that the equilibrium was in favour of enlarged presynaptic structure formation upon infection. To further confirm this observation, we showed that mRNA expression of Bassoon, FLRT3 and vesicle transport through interaction with t-SNAREs homolog 1B (VTI1B), three presynaptic components, was significantly up-regulated in patients with COVID-19. Mechanistically, we found that LPHN3, the post-synaptic G-protein coupled receptor (GPCR) of FLRT3[28], which is involved in excitatory synapse formation and maintenance[29], was also overexpressed upon SARS-CoV-2 infection in cerebral organoids, ex vivo infected OPAB and in post-mortem cortical samples from individuals with COVID-19. Treatment with Stachel, a 12-amino-acid peptide derived from an extracellular region of LPHN3 and a LPHN3-specific agonist[30], fully reverted the presynaptic enlargement phenotype induced by the virus. Moreover, we provide functional evidence that SARS-CoV-2 perturbs organoid electrical activity using a dedicated machine learning framework, which could be partially rescued by Stachel treatment, further highlighting the important role of LPHN3 in the SARS-CoV-2-mediated synapse dysfunction. Finally, we show by quantitative live cell imaging that SARS-CoV-2 particles (or virions) accumulate and dwell at LPHN3–FLRT3 trans-synaptic sites, suggesting that local hindrance could contribute to synaptic dysfunction.

Results

SARS-CoV-2 infection of cerebral organoids

To investigate the impact of SARS-CoV-2 on neural processes, we first used cerebral organoids derived from human stem cells, which recapitulate an embryonic cortex that shows complex 3D organization of multiple cell types, including neural progenitor cells (NPCs), post-mitotic neurons and astrocytes (Fig. 1a and Extended Data Fig. 1a). Evaluation of the permissiveness of this model to SARS-CoV-2 carried out by confocal image quantification and real-time quantitative polymerase chain reaction (RT-qPCR) showed some heterogeneity, ranging from barely to highly infected status (Fig. 1b,c and Extended Data Fig. 1b–d). This result is reminiscent of the variability previously reported in cerebral organoid models[17]. Furthermore, SARS-CoV-2 RNA levels were found to be low in organoids as monitored by RT-qPCR using N1 primers (Extended Data Fig. 1c). Subgenomic RNA (sgRNA) quantification, showing only the viral RNA that was replicated, showed low but consistent replication over time, confirming that SARS-CoV-2 replicates slowly and at low levels in organoids (Extended Data Fig. 1d). In agreement with this observation, almost no infectious particles were detectable in the supernatant of organoids and in dissociated organoid homogenates, as quantified by plaque assay using Vero E6 cells (Extended Data Fig. 1e), further indicating that virus propagation in the organoid is relatively inefficient. Analyses of the impact of SARS-CoV-2 infection on the viability of cerebral organoids showed no significant cytotoxicity, apoptosis or organoid growth defect (Extended Data Fig. 1f–h). As previously reported, we confirmed that neurons were the most permissive cell type for the virus (Extended Data Fig. 1i), although SARS-CoV-2 cellular neurotropism is a complex question that is still debated[31–34].

Together, our data indicate that SARS-CoV-2 can infect cerebral organoids, although they are poorly permissive to viral dissemination.

Single-organoid proteomic analyses of SARS-CoV-2 infection

To gain further insights into the molecular impact of SARS-CoV-2 infection, we performed differential proteomic analyses on single cerebral organoids in the presence/absence of virus using nanoscale liquid chromatography coupled to tandem mass spectrometry (nanoLC-MS/MS; Fig. 1d). Protein ontology analyses revealed that SARS-CoV-2 exposure led to strong up-regulation of proteins associated with neural projections and synaptic signalling (Fig. 1e, Extended Data Fig. 2a and Supplementary Table 1). Using the Synapse Gene Ontologies software (SynGO, v1.2)[35] on the 180 proteins up-regulated upon infection with $P < 0.05$ and fold change >2 (Mock versus 10^5 CoV), we found that about a third of them were part of the synaptosome, while down-regulated proteins did not lead to significant synapse-related modulation (Fig. 1e–g). Our proteomic dataset also allowed us to map the post-translational modifications (PTMs) associated to SARS-CoV-2 infection in organoids, including the deamidation of the asparagine at position 29 of the SARS-CoV-2 nucleocapsid (N) protein (Extended Data Fig. 2b–d and Supplementary Tables 1 and 2).

We next monitored by confocal microscopy whether the synaptic protein enrichment identified by mass spectrometry could be observed in individual organoids. Quantitative image analyses of the presynaptic marker Bassoon in organoids highlighted that these structures were significantly enlarged and elongated upon exposure to SARS-CoV-2 in a dose-dependent manner (Fig. 2a–f). It remains uncertain whether these elongated objects correspond to single long presynaptic structures or to multiple juxtaposed objects, as our imaging resolution might not be sufficient to segregate synapses too close to each other.

Synaptic enlargement is reverted upon monocyte infiltration

Our observation that synaptic proteins are up-regulated upon SARS-CoV-2 infection of cerebral organoids are not in agreement with previous studies suggesting that synapses can be pruned by microglial cells[26,36]. Because protocol of cerebral organoid production does not lead to microglial differentiation, we supplemented our cerebral organoids with human monocytes that readily infiltrated organoids, staining positive for Iba-1, CD163 and CD206 (Extended Data Fig. 3a,b), markers of microglia/macrophage cells. In organoids

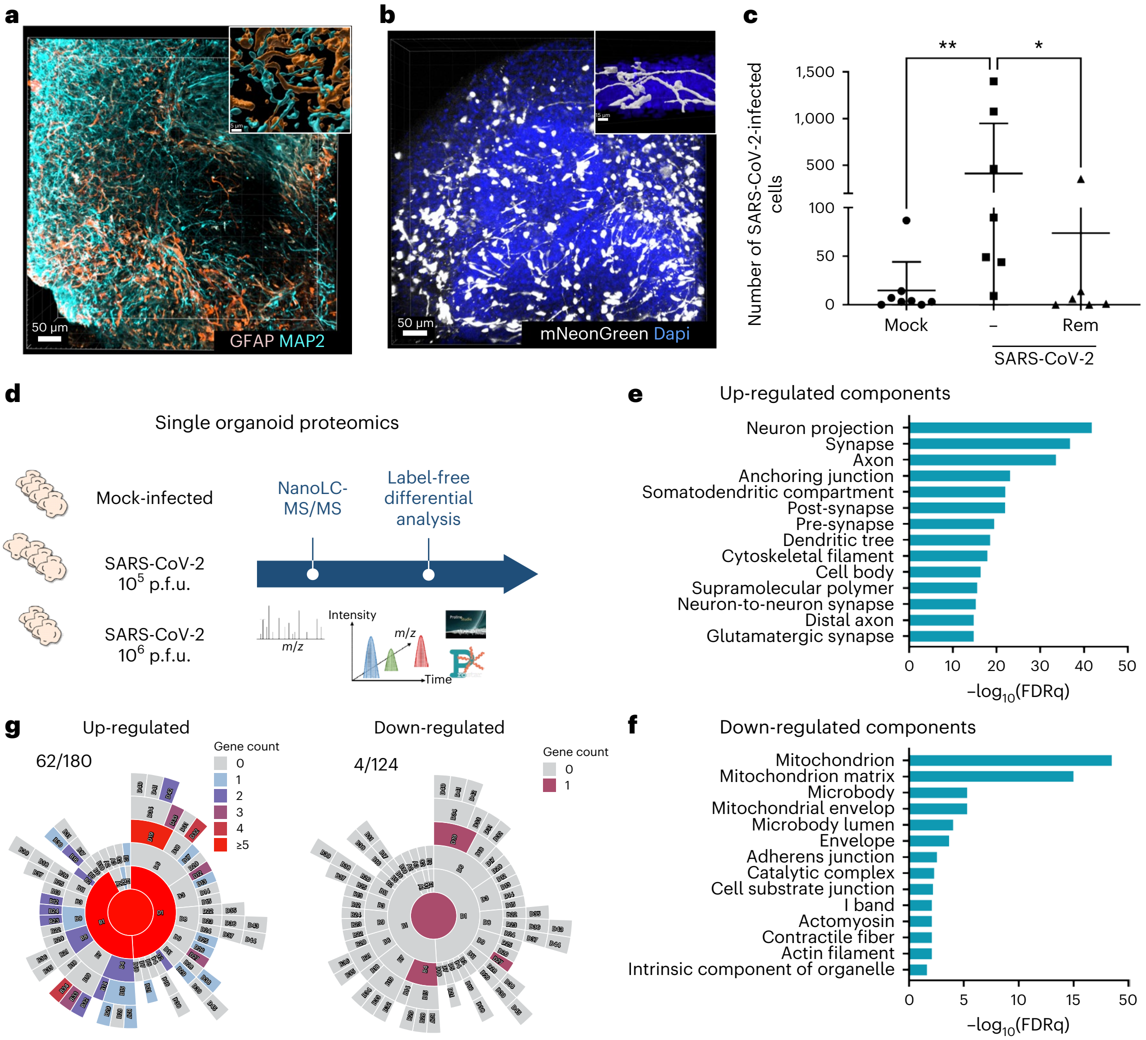

Fig. 1 | SARS-CoV-2 infection of cerebral organoids induces an increase in synapses protein expression. a, Three-dimensional snapshots of cerebral organoids differentiated for 45 days stained for post-mitotic neurons (MAP2, cyan) and astrocytes (GFAP, orange). **b**,**c**, Cerebral organoids were mock-infected or infected for 10 days with SARS-CoV-2 mNeonGreen at 10^5 p.f.u. per organoid in the absence or presence of 10 µM Remdesivir. **b**, Micrograph of organoid (white) and nuclei (blue) highly infected with SARS-CoV-2. **c**, The number of infected cells from eight individual organoids per condition. Two-tailed *P* values (Kruskal–Wallis test), $^{**}P < 0.0039$, $^{*}P = 0.0452$. Data are presented as mean ± s.d. **d**–**g**, Infected organoids differentiated for 45 days were processed for single-organoid differential proteomics comparing infected organoids to their non-infected counterparts using nanoLC-MS/MS. **d**, Schematic representation of the workflow. **e**,**f**, Protein ontology analysis using gene set enrichment analysis of the cellular component up-regulated (**e**) or down-regulated (**f**) upon infection of cerebral organoids. **g**, The up-regulated and down-regulated proteins were analysed using SynGo database and diagrams were built based on the synaptic distribution of the proteins belonging to the synaptosome.

devoid of infiltrated monocytes, we found that SARS-CoV-2 significantly increased the size of the presynaptic marker Bassoon at 3 and 10 days post-infection (d.p.i.; Fig. 2g and Extended Data Fig. 3c). By contrast, however, we found in organoids containing infiltrated monocytes that SARS-CoV-2 was decreasing Bassoon object size at 10 d.p.i. In this model, we could indeed observe that the infiltrated monocytes contained elongated synaptic structures (Fig. 2h), in accordance with previous reports that microglia may play an important role in synaptic pruning upon SARS-CoV-2 infection.

SARS-CoV-2 infects human brain explants to a low extent

Cerebral organoids are immature brain surrogates with high neuronal plasticity. Their supplementation with infiltrated monocytes remains relatively artificial and does not recapitulate the cell density and ratio of an adult human brain. In particular, it is unclear whether the synaptic pruning observed would also occur in a more physiologic cortical model system. To better represent the 3D architecture, cellular diversity and neural microenvironment of the adult cortex, we used another approach based on the OPAB obtained from individuals without COVID-19 (Supplementary Table 3) to assess the impact of SARS-CoV-2 on synaptic components. Ex vivo infection of parietal and frontal OPAB with SARS-CoV-2 reporter viruses[37] highlighted that a marginal number of cells could be infected, and the virus could replicate but not significantly propagate into the slice over time (Extended Data Fig. 4a–d). Moreover, the addition of SARS-CoV-2 to the slices did not result in toxicity or major tissue disorganization (Extended Data Fig. 4e,f). These data reinforce our findings that SARS-CoV-2 has the ability to infect neural cells but to a very low extent.

SARS-CoV-2 increases presynaptic component expression in OPAB

We next assessed the impact of SARS-CoV-2 on presynaptic components using the ex vivo OPAB model. We found that Bassoon object size was significantly increased upon infection, showing similar elongated structures as seen in infected organoids (Fig. 3a–c). To further strengthen this finding in most natural infection conditions, we obtained cortical brain samples from six patients who died from non-neurological COVID-19 (Supplementary Table 3). We found that two patients (P3 and P6) had detectable SARS-CoV-2 RNA levels (using the N1 primers) in the temporal lobe of the cortex without correlation with the viraemia and viral load in the blood and cerebrospinal fluid (Fig. 3d and Extended Data Fig. 5a). It is noteworthy that SARS-CoV-2 infection of OPAB leads to viral RNA expression levels (using the N1 primers) that are similar to the naturally infected samples (patients P3 and P6; Fig. 3d; ex vivo infection "INF ex vivo explant" condition), suggesting that our ex vivo infection model reproduces physiological brain infection levels found in patients' brain. Initial clinical PCR analysis found SARS-CoV-2 RNA (using IP2 and IP4 primers[38]) in the temporal lobe of patients P1 and P6, suggesting that we are close to the limit of detection of the PCR, and one can assume that the cortex of all patients might contain trace amount of SARS-CoV-2 RNA, depending on the subregion from which the RNA was extracted. It is noteworthy that it is unlikely that the viral RNA detected in the brain originates from the blood, as sample preparation includes washes and negligible amount of vascularization over tissue (ref. 39), and in several patients, the viraemia was undetectable (Extended Data Fig. 5a).

In these brain samples from patients with COVID-19, we found several clusters of cells positive for viral protein nucleocapsid (N) or spike (S) with morphological features of neurons in the frontal and parietal lobes of patient P3 (Fig. 3e), which further highlights that depending on the location analysed, SARS-CoV-2 infection may be detected in the brain of patients with COVID-19, even in the absence of obvious neurological symptoms. Moreover, these data are important because patient P3 had no neurological symptoms reported, although it cannot be excluded that subtle cognitive or psychiatric dysfunctions remained undetected. It is noteworthy that there was no detectable infiltration of leukocytes in any of these patients or significant astrogliosis (Fig. 3f and Extended Data Fig. 5b,c). Moreover, CD163 and CD68 stainings were mostly absent, except in blood vessels (Extended Data Fig. 5d), suggesting that no overactivated microglia were present.

RT-qPCR analysis of the mRNA expression of Bassoon in the temporal lobe of patients who died from non-neurologic COVID-19 was significantly increased compared to individuals who died of non-COVID causes (Fig. 3g and Extended Data Fig. 6a). Unfortunately, we failed to analyse these patient samples by western blot (Bassoon is a 420 kDa protein). It is worth noting that the Bassoon mRNA overexpression was not correlated to the amount of viral RNA detected, suggesting that brain exposure to low amount of SARS-CoV-2 might be sufficient to trigger abnormal Bassoon expression. By contrast, the mRNA coding for the post-synaptic marker post-synaptic density protein 95 (PSD95) was not modulated in patients with COVID-19 (Fig. 3h and Extended Data Fig. 6b). We also report that the mRNA coding for the post-synaptic AMPA receptor glutamate receptor 2 (GluA2) was not modulated in patients with COVID-19, while the presynaptic secretion modulator VTI1B was significantly up-regulated (Extended Data Figs. 5f–g and 6c,d). Finally, we showed that this effect was not strain dependent as organoid infection with the Delta strain of SARS-CoV-2 similarly induced presynaptic enlargement (Extended Data Fig. 5h). Together, our data highlight that exposure to SARS-CoV-2 is associated to the increase in presynaptic components in the human cortex.

LPHN3 is up-regulated upon brain exposure to SARS-CoV-2

To further investigate the functional relevance of the abnormal expression and morphology of presynaptic components, we looked at individual proteins found consistently overexpressed in our proteomic dataset. Latrophilin-3 (LPHN3 protein coded by the *ADGRL3* gene) caught our attention, as it is a post-synaptic GPCR involved in synapse formation and maintenance[29,40,41] and is the most up-regulated protein upon infection identified in organoids (Fig. 4a and Supplementary Table 1). Moreover, LPHN3 protein was up-regulated in OPAB exposed to SARS-CoV-2 (Fig. 4b,c), and the mRNA coding for LPHN3 was also increased in the COVID-19 brain samples compared to non-COVID-19 samples (Fig. 4d and Extended Data Fig. 6e). The mRNA coding for FLRT3, the main receptor of LPHN3[28], was also up-regulated in patients with COVID-19 (Fig. 4e and Extended Data Fig. 6f). To test whether this increase had functional consequences, we measured LPHN3-dependent cyclic adenosine monophosphate (cAMP) production in mock- or SARS-CoV-2-infected cells using the SVG-A astroglial cell line engineered to overexpress Angiotensin-converting enzyme 2 (ACE-2), allowing permissiveness to SARS-CoV-2 (Extended Data Fig. 7a,b). The SVG-A ACE-2 cells represent a good tool to study SARS-CoV-2 infection in neural cells, complementary to other neural cell lines[42], as they are very permissive and easy to transfect. Moreover, SVG-A cells express endogenous levels of LPHN3 and FLRT3 and are responsive to Stachel, an agonist peptide specific for LPHN3-dependent cAMP expression activation (ref. 30 and Extended Data Fig. 7c,d). In these cells, we found that SARS-CoV-2 significantly increased Stachel-induced cAMP levels, even in UV-inactivated samples (Fig. 4f). In cerebral organoids, we showed that Stachel treatment also led to increased cAMP production (Extended Data Fig. 7e) and that it potently reverted the phenotype of presynaptic enlargement induced by SARS-CoV-2 toward significantly smaller synapses (Fig. 4g,h), indicating that virus-induced presynaptic abnormalities are LPHN3 dependent.

Fig. 2 | SARS-CoV-2 exposure increases the number of presynaptic structures in cerebral organoids. a–e, Cerebral organoids were mock-infected or infected for 10 days with SARS-CoV-2 mNeonGreen at 10^5 p.f.u. per organoid. Organoids were fixed and stained for the presynaptic marker Bassoon. **a**, Micrographs highlight the abnormal elongated shape of the Bassoon marker. The lower right insets represent colour-coded Bassoon signal based on the size of the objects, below 0.8 μm^3 (cyan) or above (purple). **b–e**, Quantifications of the Bassoon signal from **a**. **b**, Sphericity index of object above 0.8 μm^3, highlighting that SARS-CoV-2 infection correlates to elongated presynaptic Bassoon structures. The *n* corresponds to the number of objects from one organoid. Two-tailed *P* value from unpaired *t*-test, ****$P < 0.0001$. **c**,**d**, The distribution of Bassoon object volumes for each condition. **c**, The *n* corresponds to single Bassoon objects obtained from one organoid. Two-tailed *P* value from unpaired *t*-test, ****$P < 0.0001$. Each dot corresponds to single Bassoon objects obtained from one organoid. **d**, The binning of the Bassoon objects by volume highlights a marked increase in the number of Bassoon objects of 2 μm^3 and above. **e**, Quantification of the percentage of Bassoon objects >2 μm^3. Each dot corresponds to fields of view acquired from $n = 3$ organoids. Two-tailed *P* value from unpaired *t*-test, **$P = 0.002$. Data are presented as mean ± s.d. **f**, Cerebral organoids differentiated for 45 days were mock-infected or infected for 10 days with SARS-CoV-2 at 10^3 p.f.u. or 10^5 p.f.u. per organoid. The graph shows the distribution of bassoon object volumes for each condition. Each dot corresponds to a single bassoon object obtained from *n* of two cerebral organoids per condition. Two-tailed *P* values from unpaired *t*-test, *$P < 0.0221$, ***$P < 0.001$, ****$P < 0.0001$. Data are presented as mean ± s.e.m. **g**,**h**, Cerebral organoids differentiated for 45 days were co-cultured with or without human blood monocytes for 7 days, resulting in the infiltration of the monocytes within the organoid (see associated Extended Data Fig. 3). **g**, The samples were then infected for 3 days or 10 days with SARS-CoV-2 at 10^5 p.f.u. per organoid, fixed and stained with anti-Bassoon antibodies. The graphs show the distribution of Bassoon object volumes for each condition. Each dot corresponds to single Bassoon objects obtained from one organoid. Two-tailed *P* value from unpaired *t*-test, $P = 0.5172$ (NS), ***$P < 0.001$, ****$P < 0.0001$. **h**, The samples were infected for 10 days with SARS-CoV-2 at 10^5 p.f.u. per organoid, fixed and stained with anti-Homer-1 antibodies. The micrograph illustrates Homer-1 aberrant synapses (red) inside infiltrated monocytes pre-stained with Celltrace Yellow (purple). Nuclei are stained with Dapi (grey).

SARS-CoV-2 exposure perturbs local electric field potential

Synaptic dysfunction could be consistent with the EEG abnormalities reported in patients with COVID-19 during the acute phase, but also once the infection has apparently resolved[22–24]. Consistently, our proteomic dataset identified the ontology term 'EEG abnormality' among the up-regulated proteins of interest (Extended Data Fig. 2a). To directly assess the impact of SARS-CoV-2 exposure on neural electrical activity, we performed local field potential (LFP) measurement of cerebral organoids using commercial 3D microelectrode arrays (3D MEAs) (Extended Data Fig. 8a,b). Non-infected or SARS-CoV-2-infected single organoids were plated onto 3D MEAs, and spontaneous electrical activity was recorded. Data processing was performed using a custom-made machine learning framework to identify virus-induced electrical feature modulation. Using random forest classifier (RFC), we found that organoids exposed to SARS-CoV-2 could be readily discriminated from their mock counterparts based on their LFP (Fig. 4i and Extended Data Fig. 8c). The confusion matrix in Fig. 4i shows that the electrical signal obtained from the mock recording was correctly classified 80 times while misclassified 5 times. The confidence upon prediction indicates that in the 80 correct classifications, the algorithm's confidence is 0.867

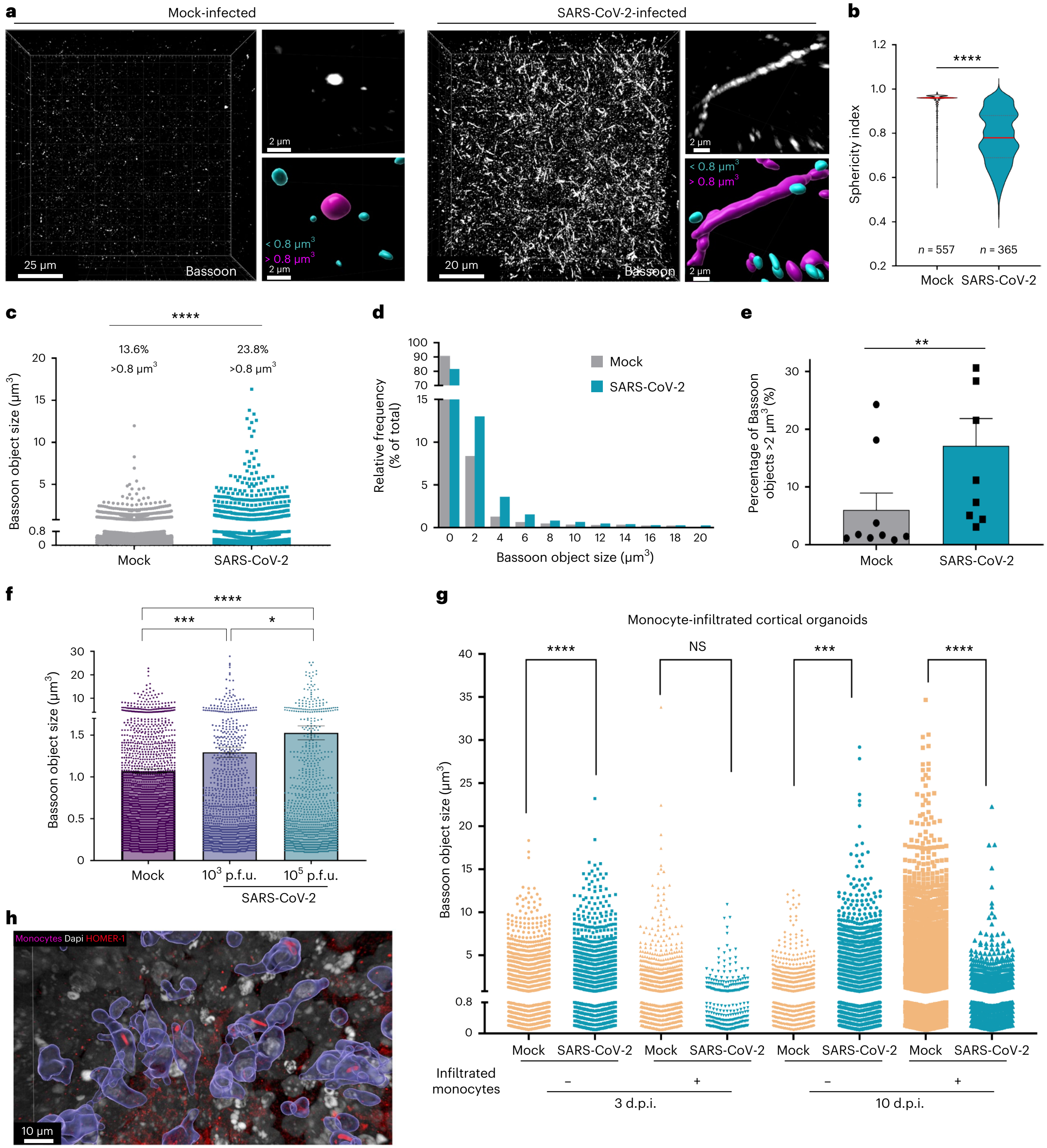

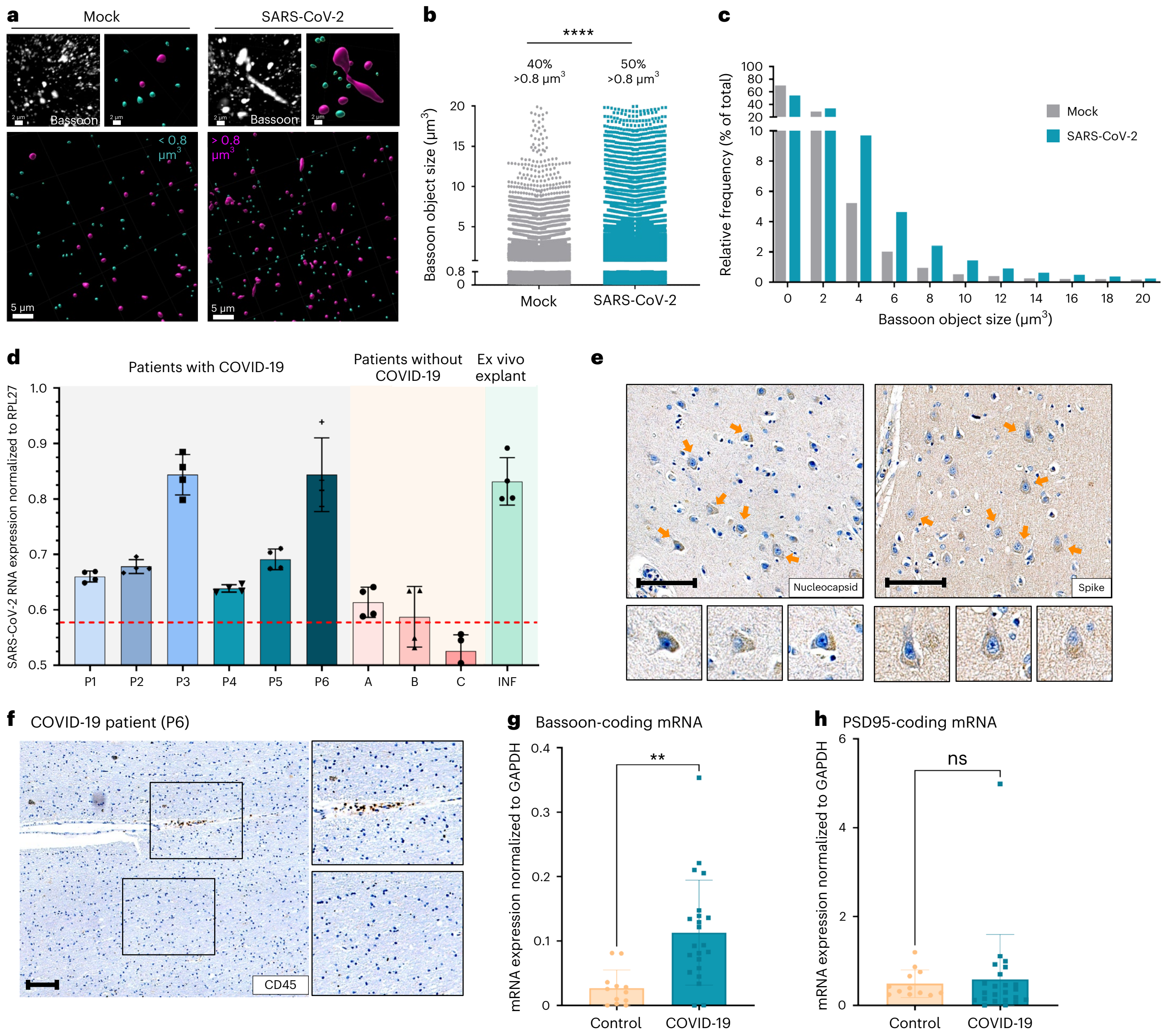

Fig. 3 | SARS-CoV-2 exposure increases presynaptic components in human brain samples. a–**c**, Organotypic ex vivo culture of post-mortem adult human brain slices (OPAB) mock-infected or infected with SARS-CoV-2 at 10^5 p.f.u. per well. **a**, OPAB were stained for the presynaptic marker Bassoon and imaged by 3D confocal microscopy. **b**, The distribution of Bassoon object volumes for each condition from the quantified images in **a**. Each dot corresponds to single Bassoon objects obtained from *n* of two brain slices from two different donors. Two-tailed *P* value from unpaired *t*-test, ****$P < 0.0001$. **c**, Quantification from **b** was plotted as binning of the Bassoon objects by volume. The graph highlights an increase in the number of Bassoon objects of 4 µm^3 and above. **d**, RNA was extracted from samples obtained from the temporal lobe of six patients with COVID-19 (patients P1–P6) who did not present neurological symptoms or individuals without COVID-19 (**a**–**c**), and RT-qPCR was performed. The data correspond to SARS-CoV-2 RNA levels normalized by the large ribosomal subunit protein eL27 (RPL27) housekeeping gene of the condition INF (ex vivo explant) of brain slices from individuals without COVID-19 that were infected with 10^5 p.f.u. SARS-CoV-2 ex vivo for 10 days. The bar graph represents mean ± s.d. for each donor, and each dot corresponds to duplicates from two experiments. The red line corresponds to the average background level of SARS-CoV-2 RNA detection in non-infected brain slices. **e**,**f**, Immunochemistry of nucleocapsid and spike from a frontal and parietal lobe of patient with COVID-19 (patient P3) (**e**) and CD45 staining (leukocyte) of patient with COVID-19 (patient P6) (**f**). Scale bars, 100 µm. The images are representative of at least six fields of view. **g**,**h**, RNA extraction and RT-qPCR from the temporal lobe of patients with COVID-19 or individuals without COVID-19 (control) were performed, and the data correspond to the mRNA levels coding for Bassoon (**g**) and PSD95 (**h**), normalized by GAPDH. Each dot corresponds to an individual measurement obtained from *n* of two individual explants collected from three individuals without COVID-19 (control) and six patients with COVID-19. Data are presented as mean ± s.d. Two-tailed *P* value from unpaired *t*-test, **$P = 0.0013$, $P = 0.7527$ (NS).

(1 being 100% confidence and 0.5 being random classification). By contrast, the confidence upon prediction for the 5 misclassified electrical signals was 0.589, indicating that these signals were misclassified randomly. This can be interpreted as the fact that these 5 datasets could not be well classified in any category. Overall, our prediction algorithm classifies electrical activity in mock/SARS-CoV-2 context with >90% accuracy and high confidence. The discrimination was not occurring because of inter-organoid variability, as our algorithm classified all the organoids as 'non-infected' before infection and after 30 min of exposure to SARS-CoV-2.

Stachel reverts SARS-CoV-2-induced synaptic perturbations

With the treatment using the LPHN3 agonist Stachel, we showed that the electrical activity of SARS-CoV-2-infected organoids partially reverted to a 'non-infected' phenotype (Fig. 4i,j), further supporting the importance of LPHN3 in the SARS-CoV-2-dependent perturbation of synaptic functions. It was recently shown that the SARS-CoV-2 spike protein alone causes memory impairment in mice[43], and here, we showed that the impact of the addition of recombinant spike on organoids induced an intermediate outcome, in-between mock and infected LFP profiles (Extended Data Fig. 8d,e), suggesting that spike may participate, but is not sufficient, to explain the SARS-CoV-2-induced neural perturbations.

SARS-CoV-2 virions dwell at trans-synaptic sites

Our data in Fig. 4f suggested that the sole exposure of neural cells to UV-inactivated SARS-CoV-2 was sufficient to induce LPHN3-dependent cAMP production. The protein FLRT3 was identified in a BioID proximity labelling assay (PLA) overexpressing individual SARS-CoV-2 proteins to be associated to the viral protein spike[44]. Unfortunately, we have been unable at this stage to show interactions between FLRT3 and spike in primary neurons by co-immunoprecipitation, while ACE-2 successfully pulled down (Extended Data Fig. 9a). The transient, indirect and/or low-affinity interaction between spike and FLRT3 could explain this result. Nevertheless, we could use PLA imaging to highlight that SARS-CoV-2 particles were indeed in close proximity to FLRT3 structures (Fig. 5a). Using UV-inactivated fluorescent SARS-CoV-2 virions[45], we observed an accumulation over time of virus at trans-synaptic sites positive for presynaptic molecule FLRT3 and the post-synaptic marker Homer-1 (Fig. 5b), suggesting that extracellular virions could be retained onto trans-synaptic structures in the absence of productive infection. Confocal imaging of replication-competent fluorescent SARS-CoV-2 particles showed virions at the LPHN3–FLRT3 trans-synaptic interface (Fig. 5c), and quantification of the co-localization between virions and LPHN3, FLRT3, Homer-1 and Bassoon showed a significant increase in the localization of viral particles and the various synaptic markers (Fig. 5d–g).

We reasoned that virions could get trapped at FLRT3 synaptic sites, which would in turn decrease FLRT3–LPHN3 interactions and thus perturb synaptic functions. To investigate this hypothesis, we performed confocal 3D live cell imaging on neurons derived from NPCs transduced with a FLRT3–mCherry construct (Extended Data Fig. 9b) to monitor the dynamics of virus–FLRT3 interactions in real time. Upon incubation of neurons with SARS-CoV-2 N-mNeonGreen fluorescent virions, we observed static particles associated to FLRT3 structures at the plasma membranes of neurons (Fig. 5h and Supplementary Video 1). However, the overexpression of FLRT3 may provide artefactual interactions, and we also observed abnormal accumulation of FLRT3–mCherry within the cell. To circumvent this issue, we used SynaptoRed, a dye enriched in synaptic regions, to measure the association of viral particles with synaptic structures. We observed that SARS-CoV-2 virions found at synapses (Fig. 5i–k particle A and associated Supplementary Video 2) showed relatively static and constrained movements, while viral particles at the surface of neurons but devoid of the SynaptoRed marker had greater dynamics (Fig. 5i–k particle B and associated Supplementary Video 3). Quantitative analysis of these observations revealed a significant inverse correlation between the speed of the virions and the amount of SynaptoRed signal (Fig. 5l–m). Indeed, 12.5% of the tracks that show no/low SynaptoRed are dynamic (>0.1 µm s^{-1}), while only 5.3% of the tracks with SynaptoRed are mobile (Fig. 5l, dynamic tracks). These data further confirm that SARS-CoV-2 particles steadily dwell at synaptic sites.

Discussion

NeuroCOVID remains insufficiently understood at the molecular and subcellular levels. Although hypoxia and neuroinflammation may be important processes involved in severe neuroCOVID, it cannot fully explain subtle neurological and/or psychiatric disorders in patients with mild COVID-19 in the acute and post-acute phases. The virus has been shown to persist at low levels in the brain of patients with COVID-19 for long periods of time[16], but the dynamics and impact of SARS-CoV-2 particles in the CNS remain unknown. Here we show that exposure to SARS-CoV-2 can perturb neuronal synapse morphology, modulate the synaptosome landscape and interfere with local electrical field potential.

We used a combination of models and samples, including cerebral organoids, OPAB and patient samples. Although several studies described the virologic aspects of brain infection in brain organoids[17], we also compared this model to OPAB, to better represent an adult brain (cell composition, 3D architecture, mature differentiation and so on). Indeed, the OPAB model has the advantage of being of human and adult origin, to frequently be provided with large amount of primary biological material. These practical, physiological and scalable features are major advantages over organotypic culture of brain explants obtained from surgery, which are rare, in small amount and coming from patients with severe neurological disorders (justifying brain resection).

Fig. 4 | LPHN3 is up-regulated upon SARS-CoV-2 infection and is associated with synapses dysregulation. a, Cerebral organoids differentiated for 45 days were mock-infected or infected for 10 days with SARS-CoV-2 at 10^5 p.f.u. or 10^6 p.f.u. per organoid and processed for single-organoid differential proteomics. Heat map by single-organoid differential proteomics. The heat map of the up-regulated proteins shows the colour-coded fold change (FC) of SARS-CoV-2 exposure for each individual organoid at 10^5 p.f.u. and 10^6 p.f.u. The most enriched protein in the infected samples (>20-fold) is the viral Matrix (M), followed by the post-synaptic host protein ADGRL3 (LPHN3), up-regulated >6-fold. **b**,**c**, Organotypic ex vivo culture of post-mortem human frontal brain slices mock-infected or infected with SARS-CoV-2 at 10^5 p.f.u. per well for 4 days. **b**, The slices were individually lysed, and immunoblotting analysis for LPHN3 and actin as a loading control was performed. The western blot is representative of at least two individual experiments. **c**, Three-dimensional imaging of slices labelled with an anti-LPHN3 antibody. The insets highlight the shape of elongated cellular structures (upper panels) and the intensity of the LPHN3 signal (lower panels). **d**,**e**, RT-qPCR on the temporal lobes from six patients with COVID-19 and three individuals without COVID-19 in duplicates was performed, and the data correspond to the mRNA level coding for LPHN3 (**d**) or FLRT3 (**e**) normalized by GAPDH. Two-tailed *P* value from unpaired *t*-test, $^{*}P = 0.0111$, $^{***}P = 0.0002$. Data are presented as mean ± s.d. **f**, SVG-A ACE-2 cells were infected with mock, 10^5 p.f.u. SARS-CoV-2, or 10^5 p.f.u. of UV-inactivated SARS-CoV-2. The dot plot shows the levels of cAMP expression upon treatment with 100 µM Stachel; $n = 3$ individual experiments. Data are presented as mean ± s.d. Two-tailed *P* value from unpaired *t*-test, $^{****}P < 0.0001$. **g**–**j**, Cerebral organoids differentiated for 45 days were mock-infected or infected for 10 days with SARS-CoV-2 at 10^5 p.f.u. per organoid, treated or not with 50 µM of Stachel peptide. **g**, The micrograph represents elongated Bassoon structures upon infection which are not present in Stachel-treated samples (50 µM). **h**, The graph shows the distribution of Bassoon object volumes for each condition. Each dot corresponds to single Bassoon objects obtained from one organoid. Two-tailed *P* value from unpaired *t*-test, $^{****}P < 0.0001$. **i**,**j**, Analyses of the LFP recorded by 3D MEA using RFC. **i**, Confusion matrix for testing the impact of Stachel. The rows represent the different outputs the RFC model has been trained to recognize. The columns represent the data we provided to the model for testing purposes. In each box are the percentages of entries classified as mock- or SARS-CoV-2-infected. The model has been trained on recordings of infected and mock condition at 24 h.p.i. and tested on recordings of infected, mock and Stachel-treated infected condition at 24 h.p.i. CUP, confidence upon prediction. **j**, Principal component analysis of mock and infected conditions at 24 h.p.i. The figure shows the first two principal components that capture the maximum variance of the electrical activity through the mock (green) and infected (blue) conditions. This same transformation was then applied to the Stachel-treated infected recordings 24 h.p.i. to analyse the activity represented along the same principal axes (red). The ellipses represent the confidence for each condition.

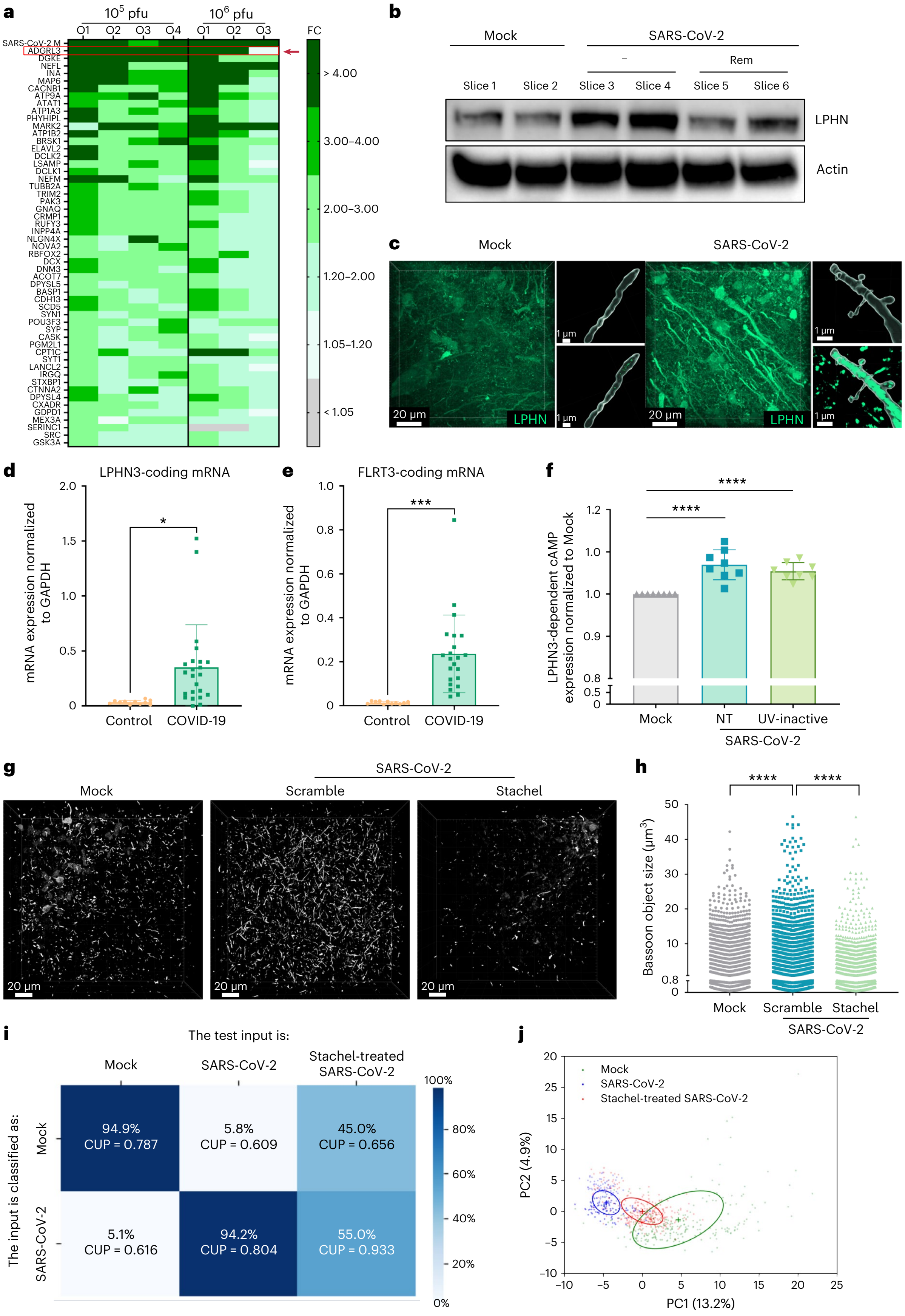
a
10^5 pfu
10^6 pfu
O1
O2
O3
O4
O1
O2
O3
FC
SARS-CoV-2 M
ADGRL3
DGKE
NEFL
INA
MAP6
CACNB1
ATP9A
ATAT1
ATP1A3
PHYHIPL
MARK2
ATP1B2
BRSK1
ELAVL2
DCLK2
LSAMP
DCLK1
NEFM
TUBB2A
TRIM2
PAK3
GNAQ
CRMP1
RUFY3
INPP4A
NLGN4X
NOVA2
RBFOX2
DCX
DNM3
ACOT7
DPYSL5
BASP1
CDH13
SCD5
SYN1
POU3F3
SYP
CASK
PGM2L1
CPT1C
SYT1
LANCL2
IRGQ
STXBP1
CTNNA2
DPYSL4
CXADR
GDPD1
MEX3A
SERINC1
SRC
GSK3A
> 4.00
3.00–4.00
2.00–3.00
1.20–2.00
1.05–1.20
< 1.05
b
Mock
SARS-CoV-2
–
Rem
Slice 1
Slice 2
Slice 3
Slice 4
Slice 5
Slice 6
LPHN
Actin
c
Mock
SARS-CoV-2
20 μm
LPHN
1 μm
1 μm
20 μm
LPHN
1 μm
1 μm
d
LPHN3-coding mRNA
mRNA expression normalized to GAPDH
2.0
1.5
1.0
0.5
0
*
Control
COVID-19
e
FLRT3-coding mRNA
mRNA expression normalized to GAPDH
1.0
0.8
0.6
0.4
0.2
0
***
Control
COVID-19
f
LPHN3-dependent cAMP expression normalized to Mock
1.2
1.0
1.0
0.9
0.8
0.5
0
****
****
Mock
NT
UV-inactive
SARS-CoV-2
g
Mock
SARS-CoV-2
Scramble
Stachel
20 μm
20 μm
20 μm
h
Bassoon object size (μm^3)
50
40
30
20
10
0.8
0
****
****
Mock
Scramble
Stachel
SARS-CoV-2
i
The test input is:
Mock
SARS-CoV-2
Stachel-treated SARS-CoV-2
The input is classified as:
Mock
SARS-CoV-2
94.9% CUP = 0.787
5.8% CUP = 0.609
45.0% CUP = 0.656
5.1% CUP = 0.616
94.2% CUP = 0.804
55.0% CUP = 0.933
100%
80%
60%
40%
20%
0%
j
Mock
SARS-CoV-2
Stachel-treated SARS-CoV-2
PC2 (4.9%)
20
25
15
10
5
0
–5
–10
PC1 (13.2%)
–10
–5
0
5
10
15
20
25

OPAB hence represents an attractive option to complement clinical studies and animal-based research.

The primary neural target of SARS-CoV-2 is mostly found to be neuronal, although other neural cell types have been reported to show some degree of permissiveness[32,33]. Interestingly, the sustained viral load we measured in organoids and brain slices suggests that some basal levels of active replication occurs, despite that no virus release in the supernatant could be detected by plaque assay. SARS-CoV-2 interacts with numerous host factors that favour virus replication, but the virus is also targeted by restriction factors, offering an evolutionary battle (for a review, see refs. 46,47), for which all cell types are not equally equipped to face. Neural cells express low levels of ACE-2, a main SARS-CoV-2 receptor[18], which could explain low permissiveness but also point toward a potential mechanism for the establishment of a CNS reservoir for the virus, as previously suggested[16]. Furthermore, we found two clusters of infected cells with the morphology of neurons in the brain of patients who died from COVID-19. These patients did not exhibit detectable signs of neurological disorders. These data are of high importance because they highlight that the CNS is a bona fide compartment for SARS-CoV-2 replication, even in the absence of neurological symptoms or strong immune responses. Indeed, our anatomopathological search for infiltrated cells failed to spot a single leukocyte in these infected regions or anywhere else in the examined tissue samples, suggesting that low levels of viral replication in the cortex may not be sufficient to elicit potent neuroinflammation. A previous report indicated that microglial activation, T-cell infiltration and astrogliosis were observed in the cortex of SARS-COV-2-infected patients with COVID-19 (ref. 25). They also could not identify SARS-CoV-2 RNA in any of the samples. In the study, the interpretations arose from single-cell RNA sequencing (scRNAseq) quantification. By contrast, a recent study reported little to no neuroinflammation in patients during acute and convalescent stages in their autopsy cohort, although they clearly showed SARS-CoV-2-infected cells in the brain[16]. Our data reinforce these observations, including the absence of leukocyte and T-cell infiltration and microglial activation.

Using single-cell transcriptomics, a few studies uncovered major neural dysregulations in patients with severe COVID-19 and in organoids[25,26]. These studies identified that synaptic signalling was perturbed upon SARS-CoV-2 infection, although the consequences of these changes remain unknown. One study identified a down-regulation of synaptic vesicle component mRNAs[25], while the other one highlighted that SARS-CoV-2 infection led to significant overexpression of genes related to synapse assembly, synaptic transmission and post-synaptic membrane potential[26]. We also observed up-regulated synaptic protein expression in patients with COVID-19, OPAB and organoids devoid of microglia. One could hypothesize that this discrepancy actually reflects a dynamic process by which virus-induced up-regulation of synaptic components leads to a concomitant opposite event: the microglia-mediated pruning of defective synapses[26,36]. Hence, we postulate that the regulation of defective synapses could be directly correlated to the amount of microglia in the vicinity of the infected cells, which would thus determine the up/down-scaling of synaptic structures. Based on Bassoon staining, we found that SARS-CoV-2 infection was associated to elongated presynaptic morphology. This observation is reminiscent of the homeostatic synaptic scaling concept, which postulates that the strength of neuronal synapses scales up in response to decreased presynaptic activity, resulting in enlarged synapse morphology[48–50].

Our in silico analysis of differential PTM from single-organoid proteomic analyses revealed the addition of an amide group to glycine as one of the most common enriched PTMs upon SARS-CoV-2 exposure. Moreover, we observed the deamidation of the asparagine 29 of SARS-CoV-2 N protein. A previous report investigated N protein PTM but did not report deamidation modifications[51], which could be explained by the different models used. Interestingly however, deamidation of the spike protein was described and associated to decreased virus-receptor fitness[52]. As deamidations has been linked to innate immune signalling[53], one may hypothesize that SARS-CoV-2 N deamidation could be the result of an intrinsic antiviral mechanism, although further research is required to understand the potential importance of this PTM.

Mutations in LPHN3 are a well-established risk factor for attention deficit hyperactivity disorder, and LPHN3 defects are also correlated to increased reward motivation and addiction, and spatial and egocentric cognitive impairments[54–58]. At the molecular level, LPHN3 is involved in the formation of both excitatory and dopaminergic synapses, interacting with FLRT3 and teneurin[28,29,55,59,60]. We highlighted that LPHN3 was one of the most up-regulated proteins in cerebral organoids infected by SARS-CoV-2 and confirmed its up-regulation at the protein level in OPAB and mRNA level in non-neurologic patients with COVID-19.

Fig. 5 | SARS-CoV-2 virions accumulate at LPHN3/FLRT3-containing synapse. **a**, Human neurons differentiated from NPCs were exposed with or without SARS-CoV-2 particles for 3 h. The micrograph shows the staining from the proximity ligation assay (PLA; yellow) using anti-spike and anti-FLRT3 antibodies and counterstained with an actin marker (phalloidin; cyan). Each yellow dot corresponds to regions where FLRT3 and the viral protein spike are closely associated. **b**, Post-mitotic neurons derived from hNPCs were mock-exposed or exposed to UV-inactivated SARS-CoV-2 for 3 or 12 h. Samples were fixed and stained for the presynaptic protein FLRT3 and the post-synaptic marker Homer-1. The micrographs (left) are representative images from at least 12 fields of view used for the quantification of the number of virions at FLRT3/Homer-1 synapses (right panel) at 3 or 12 h.p.i. Data are presented as mean ± s.d. from $n = 113$ virions (3 h) or 185 virions (12 h). Two-tailed P value from unpaired t-test was $^{*}P = 0.0206$. **c**–**g**, Human neurons differentiated from NPCs were exposed to replication-competent SARS-CoV-2 virions harbouring a mix of wild-type and fluorescent mRuby3-modified N protein for 4 h or 16 h. Cells were stained with LPHN3, FLRT3, Homer-1 and/or Bassoon as indicated. **c**, Three-dimensional imaging and zoom-ins of SARS-CoV-2-exposed neurons show a viral particle co-localizing with LPHN3 and FLRT3. (**d**–**g**). The percentage of virions containing the indicated synaptic marker at 16 h compared to 4 h post-infection. Data are from at least six fields of view, with the n corresponding to the number of considered objects per condition. The black centre line denotes the median value, while the box contains the 25th to 75th percentiles of dataset. The black whiskers mark the minimum and maximum values. Two-tailed P value from unpaired t-test, $^{*}P = 0.0352$ (**d**), $^{**}P = 0.0039$ (**e**), $^{*}P = 0.0380$ (**f**), $^{*}P = 0.0441$ (**g**). **h**, Three-dimensional live cell imaging of human neurons over-expressing fluorescent FLRT3 (pink) and exposed to SARS-CoV-2 N-mNeonGreen fluorescent virions (green) for 7 h. The snapshots were extracted from two time points from Supplementary Video 1. The white arrow indicates a fluorescent viral particle associated with a FLRT3 positive synapse. **i**–**m**, Three-dimensional live cell imaging of human neurons labelled with the synaptic marker SynaptoRed (cyan) and exposed to SARS-CoV-2 N-mNeonGreen fluorescent virions (orange) for >2 h. **i**, The snapshots were extracted from two time points from Supplementary Videos 2 and 3, highlighting two viral particles and their associated single-particle tracking. The timestamps indicate the time since the beginning of the acquisition. **j**,**k**, The speed of the viral particles as a function of SynaptoRed fluorescence intensity. While particle A (purple) has low levels of SynaptoRed (**j**) and moves rapidly (**k**), particle B (blue) is associated with high level of the synaptic marker (**j**) and dwells on there for the duration of the whole video (**k**). **l**, Dot plot showing the speed of SARS-CoV-2 virions as a function of the intensity of the SynaptoRed fluorescence intensity. The cyan square highlights the tracks that are positive to SynaptoRed. The red line corresponds to the regression curve depicting the significant inverse correlation between the speed and the amount of SynaptoRed. The data are merges from four individual videos. Two-tailed P value from simple linear regression was $^{****}P < 0.0001$. **m**, The mean ± s.e.m. of the virus particle speed obtained from 1,587 tracking datapoints with low SynaptoRed and 2,130 tracking datapoints with high SynaptoRed. The black centre line denotes the median value, while the box contains the 25th to 75th percentiles of dataset. The black whiskers mark the minimum and maximum values. Two-tailed P value from unpaired t-test, $^{****}P < 0.0001$. a.u., arbitrary units.

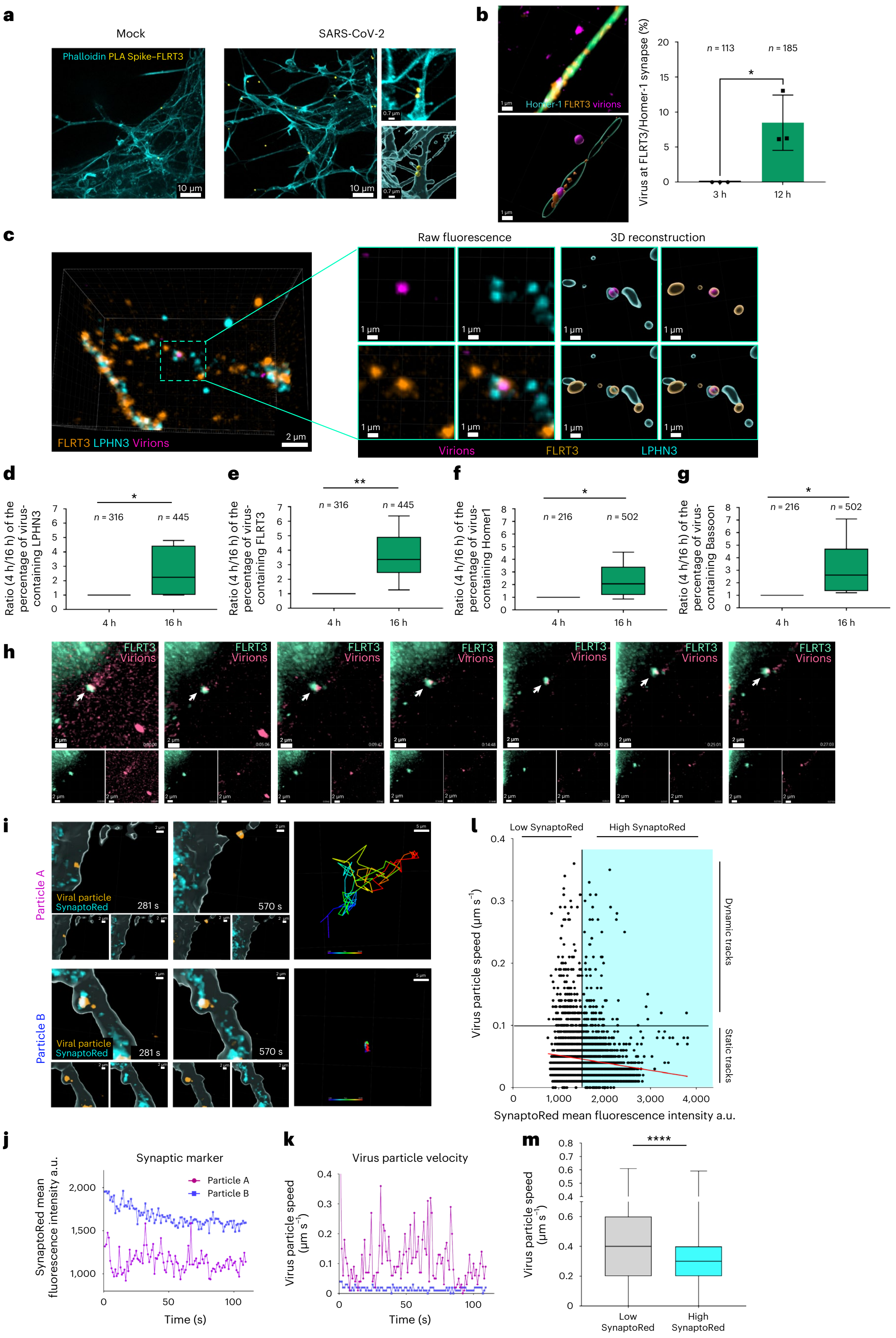
a
Mock
SARS-CoV-2
Phalloidin PLA Spike–FLRT3
10 µm
10 µm
0.7 µm
0.7 µm
b
Homer-1 FLRT3 virions
1 µm
1 µm
Virus at FLRT3/Homer-1 synapse (%)
n = 113
n = 185
*
0
5
10
15
20
3 h
12 h
c
Raw fluorescence
3D reconstruction
FLRT3 LPHN3 Virions
2 µm
1 µm
Virions
FLRT3
LPHN3
d
Ratio (4 h/16 h) of the percentage of virus-containing LPHN3
n = 316
n = 445
*
4 h
16 h
e
Ratio (4 h/16 h) of the percentage of virus-containing FLRT3
n = 316
n = 445
**
4 h
16 h
f
Ratio (4 h/16 h) of the percentage of virus-containing Homer1
n = 216
n = 502
*
4 h
16 h
g
Ratio (4 h/16 h) of the percentage of virus-containing Basson
n = 216
n = 502
*
4 h
16 h
h
FLRT3
Virions
2 µm
i
Particle A
Particle B
Viral particle
SynaptoRed
281 s
570 s
2 µm
5 µm
l
Low SynaptoRed
High SynaptoRed
Virus particle speed (µm s^{-1})
0
0.1
0.2
0.3
0.4
Dynamic tracks
Static tracks
0
1,000
2,000
3,000
4,000
SynaptoRed mean fluorescence intensity a.u.
j
Synaptic marker
Particle A
Particle B
SynaptoRed mean fluorescence intensity a.u.
1,000
1,500
2,000
0
50
100
Time (s)
k
Virus particle velocity
Virus particle speed (µm s^{-1})
0
0.1
0.2
0.3
0.4
0
50
100
Time (s)
m
****
Virus particle speed (µm s^{-1})
0
0.2
0.4
0.6
0.4
0.5
0.6
0.7
0.8
Low SynaptoRed
High SynaptoRed

LPHN3 is involved in synapse formation and maintenance through its direct interaction with the presynaptic protein FLRT3[41]. In our model, one could hypothesize that SARS-CoV-2 induces a process of 'synaptic upscaling' as a consequence of the lack of FLRT3-dependent LPHN3 activation. We hypothesize that the physical hindrance of the virion at the LPHN3–FLRT3 interface can block the normal LPHN3 activation through FLRT3 interaction and that Stachel treatment could bypass this block by activating LPHN3 independently of FLRT3 and thus restore, at least in part, synaptic function.

A BioID screening[44] and our data highlighted that FLRT3 and SARS-CoV-2 spike were in close proximity with each other. However, we were not able to evidence the interaction between the two proteins by co-immunoprecipitation. Reasons could lie in the transient nature of the interaction, that the interaction between FLRT3 and spike is too weak to be maintained during the co-immunoprecipitation procedure and/or that other factors are participating in the retention of the viral particles to synaptic buttons. Nevertheless, our live cell imaging confirmed that SARS-CoV-2 virions are retained at synaptic sites containing FLRT3. The physical retention of a virion at neuronal synapses has never been reported previously to our knowledge and offers a paradigm to explain potential viro-induced CNS perturbations. This observation could explain that transient and diverse neurological manifestations occur in patients with asymptomatic/mild COVID-19. Indeed, one could envision a scenario in which low level of SARS-CoV-2 replication in neurons induces local perturbation of the neural network through physical hindrance at the synapse, and because of the low immune response, microglial cells would take time to clear this local perturbance, leading to transient neurological symptoms. This hypothesis remains to be experimentally tested, and the specific cues involved in such processes require characterization.

We showed that SARS-CoV-2 exposure to the brain impacts electrical activity of whole organoids using 3D MEAs. LFP recording of brain organoids is very challenging to monitor. Only a few labs successfully developed approaches to monitor electrical activity in organoids (for instance, refs. 61,62), but there is no report (to our knowledge) of brain organoid electrical activity measurements that have been performed in the context of viral infection. Our workflow allows to assess the viro-induced perturbations of LFP in brain organoids in a biosafety level 3 (BSL-3) environment and could readily be extended to the study of virtually any neurotropic virus. The electrical signals recorded from brain organoids is complex and heterogenous and, thus, relatively difficult to interpret. Indeed, each electrode receives a convolved electrical signal coming from its surrounding environment, and as such, the type, number and distance of the cells to an electrode will result in diverse electrical recording outcomes. To unbiasedly compare cerebral organoid electrical activities, we developed a machine learning framework based on RFC, which gave us the best segregation capabilities for such input datasets. This approach may represent a powerful surrogate to abnormal EEGs from patients with COVID-19 (refs. 22–24). Interestingly, it was recently shown that LPHN3 null mice exhibit defective electrical activity[29], further suggesting that the SARS-CoV-2-induced modulation of LPHN3 expression and associated synapse perturbations could cause functional brain defects through neural circuitry impairments. Moreover, we made direct correlation between LPHN3 function, synaptic enlargement and electrical dysfunction using image-based quantification of synapse size and electrical activity recording. Activation of LPHN3 resulted in both cases in the (full or partial) rescue toward a non-infected phenotype. To our knowledge, LPHN3 has never been associated to a viral infection, and further research on the interplay between LPHN3 and neuroinfections could help in the development of innovative antiviral strategies.

Following up on this work, further research should establish how much our findings are contributing to knowledge on neurocognitive disorders in the context of acute infection and/or long COVID-19 and how it correlates to the severity of the disease. A 6 month follow-up study correlated COVID-19 infection to high risk of long-term neuropsychiatric disabilities[63], but whether these are linked to prolonged systemic inflammation remains unknown. We and others have not observed significant neuroinflammation in patients with COVID-19 (who did not have obvious neurological symptoms), but others did report some. Whether neuroinflammation is a transient or chronic consequence of COVID-19 infection remains unclear, yet it is critical to understand what the biological drivers governing the establishment of the so-called long COVID are. Moreover, further investigations will be needed to determine whether SARS-CoV-2 interference with LPHN3–FLRT3 signalling acts up/downstream of neuroinflammation and during acute and/or long COVID-19. Finally, correlations between the different variants of concerns, the neurological outcome and LPHN3 levels shall be investigated to evaluate whether targeting LPHN3 function could represent a mitigation strategy of interest to treat neuroCOVID symptoms.

Methods

Inclusion and ethical statement

The research presented in the study complies with all relevant ethical regulations. The protocol for post-mortem brain explants was accepted by the institutional review board of the Centre hospitalier Universitaire (CHU) Montpellier (approval ID 202000643) and the French Biomedicine Agency (agreement number PSF20-025), permitting human brain resection for research purposes during autopsy performed at the forensic institute of the CHU de Montpellier, and written family consent was obtained. For post-mortem explants of donors with COVID-19, the research protocol (Academic Hospital and University of Reims) was approved by the French Biomedicine Agency (agreement number PFS20-022). Written family consent was obtained, and absence of opposition from the patient was checked at the French Biomedicine Agency for each patient.

Antibodies and dyes

The following antibodies were used for immunofluorescence in this study: rabbit polyclonal anti-Microtubule-associated protein 2 MAP2 (1/100, GeneTex), rat monoclonal anti-B-cell lymphoma/leukemia 11B (CTIP2 or BCL11B) [25B6] (1/100, BioLegend), rabbit polyclonal anti-Pax6 (1/100, BioLegend), goat polyclonal anti-glial fibrillary acidic protein (GFAP) (1/100, Novus Biological), rabbit polyclonal anti-Iba1 (1/100, Genetex), mouse monoclonal anti-spike SARS-CoV-2 [1A9] (1/100, Genetex), mouse monoclonal anti-Bassoon [SAP7F407] (1/50, Enzo Life Sciences), rabbit polyclonal anti-Homer1 (1/50, Synaptic system), rabbit polyclonal anti-LPHN3 (1/100, Proteintech), rabbit polyclonal anti-LPHN3 (1/100, ThermoFisher), goat polyclonal anti-FLRT3 (1/50, R&D Systems), rabbit monoclonal anti-cleaved caspase 3 [5A1E] (1/100, Cell Signalling Technologies), mouse monoclonal anti-CD68 [Y1/82 A] (1/50, BioLegend), mouse monoclonal anti-CD163 [GHI/61] (1/50, BioLegend) and mouse monoclonal anti-CD206 [15-2] (1/50, BioLegend). The following antibodies were used for histology examination: mouse monoclonal anti-NeuroF [2F11](1/100, DAKO), mouse monoclonal anti-NeuN [A60] (1/400, Millipore), rabbit monoclonal anti-Oligo2 [EP112] (1/100, BioSB/diagomics), mouse monoclonal anti-GFAP [6F2] (1/400, DAKO), rabbit anti-CD3 [2GV6] (1/100, Roche), rabbit anti-spike S1 SARS-CoV-2 [ARC2373] (1/100, Diagomics) and mouse anti-Nucleocapsid SARS-CoV-2 [BSB-134] (1/750, Diagomics). The following antibodies were used for immunoblotting in this study: rabbit monoclonal anti-ACE-2 [SN0754] (1/1000, Novus Biological), rabbit polyclonal anti-Actin (1/1000, Genetex), rabbit monoclonal anti-N SARS-CoV-2 [#019] (1/1000, Sino Biological) and mouse monoclonal anti-LPHN3 [B-6] (1/500, Santa Cruz Biolotechnology). The following dyes were used in this study: Dapi nuclear counterstain (Pierce), haematoxylin and eosin, Live/Dead Viability/Cytotoxicity (ThermoFisher) and SynaptoRed C2 (Biotium).

Stem cells culture and cerebral organoid differentiation

The human embryonic stem cells (hESCs) H9 (WiCell Research Institute, WA09) were cultured and differentiated into cerebral organoids as in ref. 64. Briefly, hESCs were cultured on 60 mm Matrigel (Corning) coated plate in mTeSR PLUS media (StemCell Technologies). Cells were split by squaring colonies with a needle, and three colonies were used for a 60 mm plate. For organoid production, colonies were split onto a 100 mm plate with mitomycin-C-treated mouse embryonic fibroblast feeding layer cells in Dulbecco's modified Eagle's medium (DMEM)/F12 supplemented with Glutamax (Gibco) with 20% KnockOut serum replacement (Gibco), 1× non-essential amino acids (Gibco), 100 μM β-mercaptoethanol (Gibco) and 1× penicillin–streptomycin (Gibco). The media was changed every day with supplementation with 8 ng ml^{-1} human β-fibroblast growth factor (Sigma-Aldrich). Colonies were scooped with a cell lifter (Corning) and cultured in low binding 60 mm dish in differentiation media (hESC media supplemented with 1× sodium pyruvate). The next day, hESC differentiation was initiated by replacing half of the media with media containing 2× of the following small molecules: 3 μM IWR-1-endo, 1 μM dosomorphin, 10 μM SB-431542 and 1 μM cyclopamine, all obtained from Sigma-Aldrich. Media was renewed every other day. On day 18 post-differentiation, the growing organoids were cultured in N2 media, composed of neurobasal media (Gibco), 1× N2 supplement (Gibco), 2 mM L-glutamine (Gibco), 1× penicillin–streptomycin and 1 μM cyclopamine. On day 24, the cyclopamine was removed from the media, and organoids were grown at least until days 35 to 45 post-differentiation before being used for experiments.

Human primary monocytes purification

Buffy coats were obtained from healthy blood donors (Établissement français du sang agreement number 21PLER2019-0106) collected between 2021 and 2023, and donors should not have had COVID-19 at least for the past 14 days. All donors signed informed consent allowing the use of their blood for research purposes. Peripheral blood mononuclear cells were concentrated on a Ficoll density gradient (GE Healthcare). Monocytes were isolated by positive selection by using CD14$^+$ microbeads and magnetic columns from Miltenyi Biotec.

Co-culture of cerebral organoids with human primary monocytes

Co-culture of 500,000 human primary monocytes with 44-day-old cerebral organoids was performed for 2 days in N2 media composed of Neurobasal media (Gibco), 1× N2 supplement (Gibco), 2 mM L-glutamine (Gibco) and 1× penicillin–streptomycin. The monocytes that did not infiltrate the organoid were washed away, and the organoids were incubated for 5 more days in N2 media to allow the infiltrated monocytes to settle within the organoid. Then, organoids were fixed and stained for infiltrated monocyte characterization, and others were kept in culture for infection.

Post-mortem brain explant and ex vivo organotypic culture

All the data presented originate from 12 individuals aged from 25 to 65 years old who were all tested negative for SARS-CoV-2 by RT-qPCR of RNA extracted from nasal swabs. Individuals were chosen based on the absence of cerebral injury or trauma, and the post-mortem interval did not exceed 12 h. The frontal and parietal regions from the motor cortex were first dissected by making several 1- to 3-cm-thick coronal incisions of the brain, from frontal to occipital region, and second by cutting small cubes (about 0.5 cm^3) perpendicularly to the longitudinal axis of the gyrus and kept in N2 media at 4 °C before further processing. The cubes were embedded in 3% low melting point agarose (ThermoFisher) and sliced in 300 to 600 μm thick sections using a PELCO Easislicer (Ted Pella). All the samples show cortical layers and a piece of the white matter. The brain slices were dissociated from agarose and transferred onto cell culture inserts with 0.4 μm pore PET membranes (Millicell, Millipore) hanging in 6-well plates containing 2.5 ml of N2 media. The slices were cultured at 37 °C, 5% CO_2 and 95% humidity at the air–liquid interface, and the media was changed twice a week. Detailed characterization of OPAB can be found in ref. 27.

Patients with COVID-19

All patients (six) had a positive nasal swab for SARS-CoV-2 before death, and were hospitalized in the intensive care unit with a severe COVID-19 diagnosis, between May 2020 and May 2021, a period during which the main circulating strain in France was the SARS-CoV-2 alpha variant. Post-mortem delay before samples were taken was less than 24 h. Four male and two female patients were sampled, with a median age of 64.5 years (44 to 79 years). Delay between COVID-19 diagnosis and death was 11 to 32 days. Blood (sub-clavicular or femoral veins), and cerebrospinal fluid (lumbar puncture) was taken when possible. Samples of temporal regions of the brain lobes were immediately frozen at −80 °C, and then the brain was fixed with 4% formaldehyde. Frontal and parietal regions were sampled and embedded in paraffin. RNA samples were extracted using the KingFisher Flex systems (ThermoFisher) according to manufacturer's instructions. RT-qPCR was performed on 5 μl of RNA using the Quantabio ToughMix reagents (Quantabio). The IP2/IP4 probe sets[38] were used to detect SARS-CoV-2 RNA onsite (hospital of Reims, France). De novo RNA extraction and RT-qPCR analysis were performed later in the lab on other sections of the temporal lobe of the six patients using primer N1. Glyceraldehyde 3-phosphate dehydrogenase (GAPDH) mRNA was also quantified. Cycle threshold value (Ct) above 45 was considered negative. The Plateforme des Centres de Ressources Biologiques of the Academic Hospital of Reims stored and provided the samples for analyses at the CHU of Montpellier (n°2022-MAD30).

Neural stem cell line culture and neuron differentiation

Human neural progenitor cells (hNPCs) were obtained from Creative Biolabs (NCL-2103-P83). These cells originate from induced pluripotent stem cells obtained from adult skin fibroblasts. NPCs were cultured in flasks coated with Matrigel (Corning) with STEMdiff Neural Progenitor Medium (StemCell Technologies). Differentiation was performed on coverslips coated with 100 μg ml^{-1} poly-L-ornithine and 10 μg ml^{-1} laminin (Merck) in differentiation media (50% DMEM/F-12 + Glutamax, 50% Neurobasal, 1× N2, 1× B27). The media was changed every other day. After 8 days, 10 μg ml^{-1} brain-derived neurotrophic factor and 10 μg ml^{-1} glial cell-derived neurotrophic factor were added to the media every day until day 14, on which differentiated neurons were used for experiments.

Viruses and cells

The strain used for the in vitro studies (unless specified otherwise) is the BetaCoV/France/IDF0372/2020 isolate and was supplied by Pr. Sylvie van der Werf and the National Reference Centre for Respiratory Viruses hosted by Institut Pasteur (Paris, France). The patient sample from which strain BetaCoV/France/IDF0372/2020 was isolated in January 2020 was provided by Dr. X. Lescure and Pr. Y. Yazdanpanah from the Bichat Hospital, Paris, France. The BetaCoV/France/IDF0372/2020 was amplified in Vero E6 cells at MOI 0.001, and the supernatant was collected at 72 h post infection (h.p.i.) (when about 50% cytopathic effects were observed). Cell debris were removed by centrifugation at 2,000 × *g* for 5 min, and aliquots were stored at −80 °C. The titre was defined by plaque assays in Vero E6 cells. Typical titres were ranging around 10^7 p.f.u. ml^{-1} (plaque-forming units per millilitre). Plaque assay was performed using Vero E6 cells incubated with serial tenfold dilutions of virus in DMEM supplemented with 2% FBS, 1% P/S. The virus was adsorbed for 1 h at 37 °C with gentle plate rocking every 15 min. A 1 ml overlay (for 20 ml; 2 ml DMEM 10×, 1 ml FBS, 320 μl 7.5% $NaHCO_3$, 100 μl 1,000× P/S, 500 μl 1 M HEPES, 200 μl 100× glutamine, 10.88 ml sterile H_2O and 5 ml melted 1% agarose in H_2O) was added to each well, and plates were incubated at 4 °C for 10 min to allow agarose to form a dense gel. The plates were subsequently incubated at 37 °C for 4 days, and cells were fixed in 4% paraformaldehyde for 2 h at room temperature. Cells were then stained with crystal violet (0.1% *v*/*v* in 10% EtOH) and incubated overnight with gentle rocking. The viral titre was determined using the following formula: Number of plaques/(Dilution factor × Volume of diluted virus in ml per well) with units being plaque-forming units per millilitre. Virions were dissociated from organoids by incubating organoids in media at −80 °C followed by thawing and gentle pipetting. The resulting organoid homogenates were used to quantify infectious particles retained within the organoid (as opposed to organoid's supernatant).

SARS-CoV-2 mNeonGreen and NLuc reporter viruses (obtained from ref. 37), correspond to recombinant viruses in which the ORF7 of the viral genome was replaced with the indicated reporter gene. These replication-competent viruses express the reporter gene upon entry, replication and translation of the virus in receiving cells. The SARS-CoV-2 virions harbouring N-mNeonGreen were generated as in ref. 45. Briefly, Vero E6 cells (ECACC, Vero C1008 number 85020206), stably expressing N-mNeonGreen from SARS-CoV-2 (Addgene number 170467) were infected with wild-type SARS-CoV-2 at MOI 0.001. Titres were estimated by plaque assay. Cells were washed 24 h.p.i. with phosphate-buffered saline (PBS), the supernatant was collected at 72 h.p.i. and debris were removed by centrifugation at 2,000 × *g* for 5 min. The SVG-A cells[65] (kind gift from T. Kirchhausen) were engineered to stably overexpress human ACE-2. UV-inactivated virus was obtained by incubating 250 µl of viral preparation in a UV-C 254 nm UV chamber (Vilber Lourmat Biolink BLX UV Crosslinker) at 2 J. The loss of infectivity was confirmed by infection of Vero E6 cells. Mock-infected samples correspond to the supernatant of non-infected Vero E6 cells processed as infected cells. Remdesivir (MedChem Express) was used at 10 µM to inhibit virus replication. NLuc luminescence was measured using the Nano-Glo Luciferase Assay System (Promega) and read by PerkinElmer EnVision spectro-luminometer.

Lentivector production

HEK 293 T cells were transfected using JetPrime (Polyplus Transfection) with the three following plasmids: Gag-Pol, VSV-G and inserts of interest: either FLRT3–mCherry (obtained from Vectorbuilder (pLV[Exp]-CMV>hFLRT3[NM_013281.4]/mCherry) or hACE-2 (obtained from Dr. Caroline Goujon, Addgene plasmid number 145842)[66]. The supernatant was collected 3 days later and passed through a 0.2 µm filter (Millipore).

Immunohistochemistry

After formalin fixation and paraffin embedding, 5 µm sections were stained with haematoxylin and eosin. Immunohistochemistry was performed with Autostainer BenchMark ULTRA (Ventana Medical Systems), according to manufacturer's instructions. Briefly, paraffin sections were incubated at 60 °C for 16 min and then at 72 °C for dewaxing and at 95 °C in retrieval antigen buffer. Incubation for 30 min with antibodies was performed and revealed with 3, 3'-diaminobenzidine (DAB). Samples were washed and incubated with haematoxylin II (counterstaining) for 12 min and with bluing reagent (counterstaining) for 4 min. Images were acquired on a Leica Thunder microscope with a 3,072 × 2,048 K3C coloured camera (Leica). Mosaic acquisitions were done with a ×20 NA 0.8 air objective or ×10 NA 0.45 air objective. Images were processed with the Leica Las X software (v5.1.0).

Immunostaining of organoids and brain slices

Samples were washed with PBS once and transferred into a 96-well plate with round bottom (for brain organoids) or in 24-well plate with flat bottom (for brain slices). Samples were fixed in 4% paraformaldehyde for 1 h at room temperature. Samples were washed once with PBS and permeabilized for 24 h on a rocker with permeabilization buffer (0.5% BSA, 1% Triton in PBS). All subsequent steps were performed in permeabilization buffer. Samples were labelled with primary antibody for 24 h on a rocker, washed overnight, labelled with appropriate secondary antibodies for 24 h and washed overnight. The samples were incubated in RapiClear 1.52 reagent (Sunjin Lab) overnight at room temperature.

Fluorescence confocal microscopy

Image acquisition was performed on a spinning-disk confocal microscope (Dragonfly, Oxford Instruments) equipped with an ultrasensitive 1,024 × 1,024 EMCCD camera (iXon Life 888, Andor) and four laser lines (405, 488, 561 and 637 nm). A ×20 NA 0.8 air objective was used for whole sample imaging, and a ×60 NA 1.15 (Nikon) oil-immersion long-distance objective was used for in-depth imaging of selected areas. Images were processed using FiJi (ImageJ 1.53t) and Bitplane Imaris ×64 (Oxford Instruments) versions 9.2 and 9.7.

Live cell imaging

Neurons were differentiated on a 30-mm-diameter number 1.5 glass coverslip in six-well plates. Before imaging, the cells were incubated with SARS-CoV-2 N-mNeonGreen in neuronal media. Image acquisition was performed at 37 °C and 5% CO_2 in a dark chamber using an AxioObserver.Z1 inverted microscope (Zeiss) mounted with a spinning disc head (Yokogawa), a back-illuminated EMCCD camera (Evolve; Photometrics) and a ×100, 1.45 NA oil objective (Zeiss) controlled by MetaMorph software (v7.7) (Molecular Devices).

Image analysis and quantification

Processing and image quantification were done using Bitplane Imaris v9.7. Bassoon object was identified using absolute intensity thresholding and converted to a surface rendering model. The parameters used in this study (sphericity, volume, intensity) were automatically extracted from each object identified by intensity thresholding upon background subtraction. For virus–synapse association studies, each object was identified upon absolute intensity thresholding and converted using the 'Spot' feature on the Imaris software. A region comprising between 0 and 0.5 µm from the spot centre was used to consider that a virus particle was associated with synaptic proteins. Data were extracted automatically to excel files format. Graphs and statistics were performed using GraphPad Prism (v9).

Western blot

Samples were lysed in RIPA buffer (150 mM sodium chloride, 1% NP-40, 0.5% sodium deoxycholate, 0.1% SDS, 50 mM Tris, pH 8.0) supplemented with protease inhibitor (Promega). A pellet pestle (VWR) was used to favour protein extraction from tissues. Lysates were kept at −80 °C before analysis. Samples were spun down at 15,000 × *g* for 15 min at 4 °C; the supernatant was collected, and protein concentration was measured using a Pierce BCA Assay Kit (Pierce). A total of 10 to 20 µg of protein lysate was run on Bolt 4 to 12% Bis–Tris plus gels (ThermoFisher), and proteins were transferred to nitrocellulose membranes using iBlot2 (ThermoFisher). Nitrocellulose membranes were blocked with 5% (*w*/*v*) milk in PBST (PBS pH 7.4, 0.05% Tween 20) for 30 min. Primary antibodies were incubated for 1 h at room temperature or overnight at 4 °C in PBST containing 5% milk. Secondary antibodies were incubated for 1 h at room temperature. After washes with PBST, nitrocellulose membranes were incubated with Clarity Max Western ECL Substrate (Bio-Rad). The specific proteins were visualized with a ChemiDoc imaging system (Bio-Rad).

Immunoprecipitation

Protein lysates from neurons were incubated overnight at 4 °C with 5 µg of mouse anti-spike antibody (Genetex). The next day, 20 µl of protein G agarose beads (Pierce) was added to the lysate and incubated at 4 °C for 2 h. The beads were spun down at 3,000 × *g* for 3 min and washed three times with PBS. The sample was eluted in NuPAGE LDS sample buffer (Thermofisher) in the presence of 50 mM dithiothreitol (DTT).

RT-qPCR

All the RNA samples were extracted using the RNeasy KIT (Qiagen) according to manufacturer's instructions unless specified otherwise. RT-qPCR was performed on 2 µl of RNA using the TaqPath One-Step RT-qPCR, CG master mix (ThermoFisher). The N1 primer/probe sets designed by the Center for Disease Control were used to detect SARS-CoV-2 RNA in all experiments unless specified otherwise. For patients with COVID-19, RT-qPCR was performed using the Luna One-Step RT-qPCR Kit (New England Biolabs). Ct above 40 was considered negative. All samples were normalized to the large ribosomal subunit protein eL27 (RPL27) or GAPDH mRNA as indicated. Sequence of primers is provided in Supplementary Table 4.

Titration of cAMP

Measurement of cAMP levels was performed using the AlphaScreen cAMP Detection Kit (PerkinElmer) according to the manufacturer's instructions. Briefly, cells were seeded in 96-well plates for 24 h then mock-infected or infected with SARS-CoV-2 for an additional 24 h. Cells were stimulated with Stachel peptide (agonist) or Scramble peptide (control)—synthesized by ProteoGenix—and AlphaScreen Acceptor beads for 30 min at room temperature then treated with Biotin–cAMP and Streptavidin Donor bead for 1 h. The luminescence was read with microplate reader Envision Multilabel reader (Perkin Elmer).

MS-based quantitative proteomics

Sample preparation. Individual brain organoids were lysed in Laemmli buffer composed of 10 mM Tris pH 6.8, 1 mM EDTA, 5% SDS and 10% glycerol. Samples were sonicated for 2 min. Protein concentration of all samples was determined using the DC protein assay (Bio-Rad) according to manufacturer's instructions, in triplicate, and a standard curve was established using BSA. DTT was added at a final concentration of 50 mM, and cell lysates were heated at 95 °C for 5 min. Protein extracts were stacked in an in-house-prepared 5% acrylamide SDS–PAGE stacking gel at 50 V. Proteins in the gel were fixed with 50% ethanol/3% phosphoric acid, washed with H_2O and coloured with Silver Blue (10% phosphoric acid, 10% ammonium sulfate, 0.12% Brilliant blue G250, 20% methanol, 60% H_2O). Gel bands were cut, washed with 12.5 mM ammonium hydrogen carbonate and 50% acetonitrile (ACN), reduced with 10 mM DTT and alkylated using 55 mM iodoacetamide before overnight digestion at 37 °C with modified porcine trypsin (Promega) at a final trypsin/protein ratio of 1/50. Trypsin-digested peptides were extracted with 60% ACN in 0.1% formic acid followed by a second extraction with 100% ACN. ACN was evaporated under vacuum, and the peptides were resuspended in H_2O and 0.1% formic acid before nanoLC-MS/MS analysis.

NanoLC-MS/MS analysis. NanoLC-MS/MS analyses were performed on a nanoAcquity UltraPerformance Liquid Chromatography device (Waters Corporation) coupled to a quadrupole-Orbitrap mass spectrometer (Q-Exactive HF-X, Thermo Fisher Scientific). Peptide separation was performed on an ACQUITY UPLC Peptide BEH C18 Column (250 mm × 75 µm with 1.7 µm diameter particles) and an ACQUITY UPLC M-Class Symmetry C18 Trap Column (20 mm × 180 µm with 5 µm diameter particles; Waters Corporation). The solvent system consisted of 0.1% formic acid in water (solvent A) and 0.1% formic acid in ACN (solvent B). Samples (800 ng) were loaded into the enrichment column over 3 min at 5 µl min^{-1} with 99% of solvent A and 1% of solvent B. Chromatographic separation was conducted with the following gradient of solvent B: from 2% to 25% over 53 min, from 25% to 40% over 10 min and from 40% to 90% over 2 min.

The mass spectrometer was operated in data-dependent acquisition mode. Survey full scan MS spectra (mass range 300–1,800) were acquired in the Orbitrap at a resolution of 60 K at 200 *m*/*z* with an automatic gain control fixed at 3×10^6 and a maximal injection time set to 50 ms. The ten most intense peptide ions in each survey scan with a charge state ≥2 were selected for fragmentation. MS/MS spectra were acquired at a resolution of 15 K at 200 *m*/*z*, automatic gain control was set to 1×10^5, and the maximal injection time was set to 50 ms. Peptides were fragmented by higher-energy collisional dissociation with a normalized collision energy set to 27. Peaks selected for fragmentation were automatically included in a dynamic exclusion list for 60 s. All samples were injected using a randomized and blocked injection sequence (one replicate of each group in each block). To minimize carry-over, two solvent blank injections were performed after each sample.

Data interpretation. Raw files were converted to .mgf peaklists using MSConvert 3.0 from the ProteoWizard suite (https://proteowizard.sourceforge.io/) and were submitted to Mascot database searches (v2.5.1, MatrixScience) against a human (20,342 sequences, 2021-04-20, taxonomy ID 9606) and SARS-CoV-2 (17 sequences, 2021-04-20, taxonomy ID 2697049) protein sequences database downloaded from UniProtKB-SwissProt, to which common contaminants and decoy sequences were added. Spectra were searched with a mass tolerance of 10 p.p.m. in MS mode and 0.07 Da in MS/MS mode. One trypsin that missed cleavage was tolerated. Carbamidomethylation of cysteine residues was set as a fixed modification. Oxidation of methionine residues and acetylation of proteins *n*-termini were set as variable modifications. Identification results were imported into the Proline software (v2.6.2)[67] for validation and label-free quantification. Peptide spectrum matches (PSMs) with pretty rank equal to 1 were retained. False discovery rate (FDR) was then optimized to be below 1% at PSM level using Mascot-adjusted *E* value and below 1% at protein level using Mascot Mudpit score. For label-free quantification, extracted ion chromatograms were used to derive peptides abundances. An *m*/*z* tolerance of 10 p.p.m. was used. Alignment of the LC-MS/MS runs was performed using Loess smoothing. Cross assignment of peptide ions abundances was performed among the samples and controls using a *m*/*z* tolerance of 10 p.p.m. and a retention time tolerance of 42 s. Protein abundances were computed using the sum of the unique peptide abundances normalized at the peptide level using the median.

To be considered, proteins must be identified in all three or four replicates in at least one condition. Imputation of the missing values and differential data analysis were performed using the open-source ProStaR software (v1.30.7)[68]. Imputation of missing values was done using the approximation of the lower limit of quantification by the 2.5% lower quantile of each replicate intensity distribution ('det quantile'). A Limma moderated *t*-test was applied on the dataset to perform differential analysis. The adaptive Benjamini–Hochberg procedure was applied to adjust the *P* values and FDR.

Post-translational modification analysis

Raw mass spectrometry files were converted to mgf format using ThermoRawFileParser (v1.3.4)[69] and searched against the human complement of the UniProtKB/SwissProt protein database containing 20,397 proteins, with added common contaminants and 17 proteins from the severe acute respiratory syndrome coronavirus 2 proteome (UP000464024; June 2022). The search was performed using the ionbot search engine (v0.7.0)[70] with open modification search settings and three expected modifications: (1) carbamidomethylation of cysteine, (2) oxidation of methionine and (3) N-terminal acetylation. Results were filtered on 1% FDR using a *q* value below 0.01. A global comparison of modification levels was calculated as the ratio of ratios. In infected samples, for each modification the ratio of the number of spectra of modified versus unmodified peptides was calculated and then divided by the same ratio in the mock samples. Relative quantification was done in two steps. First, a filtering step removed PTMs that accounted for less than 3% of all PSMs detected in the sample. Second, the filtered PTMs were quantified by dividing the number of PSMs matching this PTM, by all possible modification sites of the PTM in the sample. This fraction was then normalized by the sum of all these fractions in the sample.

Electrical activity recording

Cerebral organoids were plated on 3D MEA (MultiChannel System), made of an array of 60 TiN-coated conical electrodes of 12 µm diameter active site of 80 µm height. The specific sharp shape of these electrodes allows a better penetration of the tissue than a planar MEA and the measurement of extracellular local field close to active cells. The surface of the MEA was pre-coated with 100 µg ml^{-1} poly-L-ornithine and 10 µg ml^{-1} laminin (Merck). After 2 days, electrical recording of the LFP was performed inside an incubator at 37 °C, 5% CO$_2$ and 95% humidity using the MEA2100-Mini headstage (MultiChannel System) under electromagnetic shielding. Traces of electrical signals versus time were recorded at a sampling rate of 50 kHz by the Multichannel experimenter software (v2.20) with a customized bandpass filter script for 1 min per condition.

Code development environment

This project is running on Python 3.10, on the Pycharm IDE. The versions for the main packages used for machine learning algorithms and data analysis are fiiireflyyy==0.1.19, scikit-learn==1.3.2, scipy==1.11.3 and matplotlib==3.8.1. For the complete list of requirements for the used libraries versions, refer to https://github.com/WillyLutz/electrical-analysis-sars-cov-2/blob/main/requirements.txt (ref. 71). All the required libraries have been used with the PyPI packaging tool (Pyton 3.10).

Random forest classifier specifications

The RFC is a machine learning algorithm that builds a collection of decision trees and combines their predictions to enhance accuracy and mitigate overfitting in classification tasks. As RFC, we used the sklearn.ensemble.RandomForestClassifier class from the scikit-learn python library. The used parameters are those listed by default in the documentation, at https://scikit-learn.org/stable/modules/generated/sklearn.ensemble.RandomForestClassifier.html, except for the parameter 'n_estimator' (the number of trees in the forest) initialized to 1,000. Note that the version used is scikit-learn==1.3.2.

Electrical activity analysis using machine learning

The electrical activity was recorded using an acquisition frequency of 10 kHz. Out of the 60 electrodes per recording, we selected the 35 that presented the most activity, based on the mean standard deviation of all the electrodes. We divided the 1 min electrical recordings from the infected and non-infected (mock) organoids into 30 time bins of 2 s length and performed a fast Fourier transform on each bin, thus using the frequency domain. The data were then high-pass filtered over 50 Hz. Then, we made an average out of the preselected electrodes by their standard deviation to obtain a single signal of 10,000 values using a step of 0.5 Hz. The 10,000 frequencies were down-sampled into 300 frequencies, used as features for the RFC. We used the features from 70% of the recordings made 24 h.p.i. (pulled over all infected and non-infected organoids 24 h.p.i.) to train an RFC to detect an infected recording time bin from a mock organoid time bin. We used the RFC model on the remaining 30% of the 24 h.p.i. data from each organoid—considered unseen by the model—to test the mean detectability for each organoid. The splitting of the data into a training set and a testing set (ratio 70/30) has been executed using the 'train_test_split' method from sklearn.model_selection. It splits matrices or arrays into random train and test sets, given a set size. The same RFC model (trained with 24 h.p.i. data) was also used to test the detectability of data recorded in each organoid pre-infection (0 h.p.i.) and 0.5 h.p.i. (Extended Data Fig. 8c). The test process was iterated 10 times to provide a more accurate end result. An RFC model (trained with 24 h.p.i. data) was also used to test the impact of Stachel on electrical activity. The models described here were trained on the same dataset using the same parameters and show the same performances. Thus, the model used on Stachel-treated infected data and the one used to discriminate among control and treated samples can be considered as the same model.

Statistics and reproducibility

The statistical analyses used for each experiment can be found in the associated figure legends. No statistical method was used to predetermine sample size. No data were excluded from the analyses. The experiments were not randomized. The investigators were not blinded to allocation during experiments and outcome assessment. Data distribution was assumed to be normal, but this was not formally tested.

Reporting summary

Further information on research design is available in the Nature Portfolio Reporting Summary linked to this article.

Data availability

All data are available in the main text, extended data and Supplementary Information. The plasmid coding for N-mNeonGreen and N-mRuby3 from SARS-CoV-2 is available on Addgene (number 170467 and number 170466, respectively). The mass spectrometry proteomic data have been deposited to the ProteomeXchange Consortium via the PRIDE partner repository[72] with the dataset identifier PXD036485. Source data are provided with this paper.

Code availability

The algorithm to identify infected versus non-infected organoids is available through GitHub (https://github.com/WillyLutz/electrical-analysis-sars-cov-2)[71] or upon request.

References

1. Gavriatopoulou, M. et al. Organ-specific manifestations of COVID-19 infection. *Clin. Exp. Med.* **20**, 493–506 (2020).
2. Salinas, S. & Simonin, Y. [Neurological damage linked to coronaviruses: SARS-CoV-2 and other human coronaviruses]. *Med.Sci. (Paris)* **36**, 775–782 (2020).
3. Koralnik, I. J. & Tyler, K. L. COVID-19: a global threat to the nervous system. *Ann. Neurol.* **88**, 1–11 (2020).
4. Iadecola, C., Anrather, J. & Kamel, H. Effects of COVID-19 on the nervous system. *Cell* **183**, 16–27 e11 (2020).
5. Helms, J. et al. Delirium and encephalopathy in severe COVID-19: a cohort analysis of ICU patients. *Crit. Care* **24**, 491 (2020).
6. Varatharaj, A. et al. Neurological and neuropsychiatric complications of COVID-19 in 153 patients: a UK-wide surveillance study. *Lancet Psychiatry* **7**, 875–882 (2020).
7. Rogers, J. P. et al. Psychiatric and neuropsychiatric presentations associated with severe coronavirus infections: a systematic review and meta-analysis with comparison to the COVID-19 pandemic. *Lancet Psychiatry* **7**, 611–627 (2020).
8. Nagu, P., Parashar, A., Behl, T. & Mehta, V. CNS implications of COVID-19: a comprehensive review. *Rev. Neurosci.* **32**, 219–234 (2021).
9. Baker, H. A., Safavynia, S. A. & Evered, L. A. The 'third wave': impending cognitive and functional decline in COVID-19 survivors. *Br. J. Anaesth.* **126**, 44–47 (2021).
10. Taquet, M., Geddes, J. R., Husain, M., Luciano, S. & Harrison, P. J. 6-month neurological and psychiatric outcomes in 236 379 survivors of COVID-19: a retrospective cohort study using electronic health records. *Lancet Psychiatry* **8**, 416–427 (2021).
11. Hellmuth, J. et al. Persistent COVID-19-associated neurocognitive symptoms in non-hospitalized patients. *J. Neurovirol.* **27**, 191–195 (2021).

12. Douaud, G. et al. SARS-CoV-2 is associated with changes in brain structure in UK Biobank. *Nature* https://doi.org/10.1038/s41586-022-04569-5 (2022)
13. Blazhenets, G. et al. Slow but evident recovery from neocortical dysfunction and cognitive impairment in a series of chronic COVID-19 patients. *J. Nucl. Med.* **62**, 910–915 (2021).
14. Taquet, M. et al. Neurological and psychiatric risk trajectories after SARS-CoV-2 infection: an analysis of 2-year retrospective cohort studies including 1 284 437 patients. *Lancet Psychiatry* **9**, 815–827 (2022).
15. Monje, M. & Iwasaki, A. The neurobiology of long COVID. *Neuron* **110**, 3484–3496 (2022).
16. Stein, S. R. et al. SARS-CoV-2 infection and persistence in the human body and brain at autopsy. *Nature* **612**, 758–763 (2022).
17. Ramani, A., Pranty, A. I. & Gopalakrishnan, J. Neurotropic effects of SARS-CoV-2 modeled by the human brain organoids. *Stem Cell Rep.* **16**, 373–384 (2021).
18. Song, E. et al. Neuroinvasion of SARS-CoV-2 in human and mouse brain. *J. Exp. Med.* **218**, e20202135 (2021).
19. Qian, X., Song, H. & Ming, G. L. Brain organoids: advances, applications and challenges. *Development* **146**, dev166074 (2019).
20. Hodge, R. D. et al. Conserved cell types with divergent features in human versus mouse cortex. *Nature* **573**, 61–68 (2019).
21. Brola, W. & Wilski, M. Neurological consequences of COVID-19. *Pharmacol. Rep.* **74**, 1208–1222 (2022).
22. Antony, A. R. & Haneef, Z. Systematic review of EEG findings in 617 patients diagnosed with COVID-19. *Seizure* **83**, 234–241 (2020).
23. Kubota, T., Gajera, P. K. & Kuroda, N. Meta-analysis of EEG findings in patients with COVID-19. *Epilepsy Behav.* https://doi.org/10.1016/j.yebeh.2020.107682 (2020).
24. Lin, L. et al. Electroencephalographic abnormalities are common in COVID-19 and are associated with outcomes. *Ann. Neurol.* **89**, 872–883 (2021).
25. Yang, A. C. et al. Dysregulation of brain and choroid plexus cell types in severe COVID-19. *Nature* **595**, 565–571 (2021).
26. Samudyata et al. SARS-CoV-2 promotes microglial synapse elimination in human brain organoids. *Mol. Psychiatry* https://doi.org/10.1038/s41380-022-01786-2 (2022).
27. Partiot, E. et al. Organotypic culture of human brain explants as a preclinical model for AI-driven antiviral studies. *EMBO Mol. Med.* https://doi.org/10.1038/s44321-024-00039-9 (2024).
28. O'Sullivan, M. L. et al. FLRT proteins are endogenous latrophilin ligands and regulate excitatory synapse development. *Neuron* **73**, 903–910 (2012).
29. Sando, R. & Sudhof, T. C. Latrophilin GPCR signaling mediates synapse formation. *Elife* **10**, e65717 (2021).
30. Rothe, J. et al. Involvement of the adhesion GPCRs latrop–hilins in the regulation of insulin release. *Cell Rep.* **26**, 1573–1584 e1575 (2019).
31. Ramani, A. et al. SARS-CoV-2 targets neurons of 3D human brain organoids. *EMBO J.* **39**, e106230 (2020).
32. Ferren, M. et al. Hamster organotypic modeling of SARS-CoV-2 lung and brainstem infection. *Nat. Commun.* **12**, 5809 (2021).
33. Bauer, L. et al. The neuroinvasiveness, neurotropism, and neurovirulence of SARS-CoV-2. *Trends Neurosci.* **45**, 358–368 (2022).
34. Zivaljic, M., et al. Poor sensitivity of iPSC-derived neural progenitors and glutamatergic neurons to SARS-CoV-2. Preprint at *bioRxiv* https://doi.org/10.1101/2022.07.25.501370 (2022)
35. Koopmans, F. et al. SynGO: an evidence-based, expert-curated knowledge base for the synapse. *Neuron* **103**, 217–234 e214 (2019).
36. Beckman, D. et al. SARS-CoV-2 infects neurons and induces neuroinflammation in a non-human primate model of COVID-19. *Cell Rep.* **41**, 111573 (2022).
37. Xie, X. et al. An infectious cDNA clone of SARS-CoV-2. *Cell Host Microbe* **27**, 841–848 e843 (2020).
38. Corman, V. M. et al. Detection of 2019 novel coronavirus (2019-nCoV) by real-time RT-PCR. *Euro Surveill.* **25**, 2000045 (2020).
39. Fernandez-Rodriguez, A. et al. Post-mortem microbiology in sudden death: sampling protocols proposed in different clinical settings. *Clin. Microbiol. Infect.* **25**, 570–579 (2019).
40. Burbach, J. P. H. & Meijer, D. H. Latrophilin's social protein network. *Front. Neurosci.* **13**, 643 (2019).
41. Sando, R., Jiang, X. & Sudhof, T. C. Latrophilin GPCRs direct synapse specificity by coincident binding of FLRTs and teneurins. *Science* **363**, eaav7969 (2019).
42. Bielarz, V. et al. Susceptibility of neuroblastoma and glioblastoma cell lines to SARS-CoV-2 infection. *Brain Res.* **1758**, 147344 (2021).
43. Fontes-Dantas, F. L. et al. SARS-CoV-2 spike protein induces TLR4-mediated long-term cognitive dysfunction recapitulating post-COVID-19 syndrome in mice. *Cell Rep.* **42**, 112189 (2023).
44. May, D. G. et al. A BioID-derived proximity interactome for SARS-CoV-2 proteins. *Viruses* https://doi.org/10.3390/v14030611 (2022).
45. Bakhache, W., et al. Pharmacological perturbation of intracellular dynamics as a SARS-CoV-2 antiviral strategy. Preprint at *bioRxiv* https://doi.org/10.1101/2021.09.10.459410 (2021)
46. Prasad, V. & Bartenschlager, R. A snapshot of protein trafficking in SARS-CoV-2 infection. *Biol. Cell.* https://doi.org/10.1111/boc.202200073 (2022).
47. Jouvenet, N., Goujon, C. & Banerjee, A. Clash of the titans: interferons and SARS-CoV-2. *Trends Immunol.* **42**, 1069–1072 (2021).
48. Silva, M. M. et al. MicroRNA-186-5p controls GluA2 surface expression and synaptic scaling in hippocampal neurons. *Proc. Natl Acad. Sci. USA* **116**, 5727–5736 (2019).
49. Schanzenbacher, C. T., Langer, J. D. & Schuman, E. M. Time- and polarity-dependent proteomic changes associated with homeostatic scaling at central synapses. *Elife* **7**, e33322 (2018).
50. Dubes, S. et al. miR-124-dependent tagging of synapses by synaptopodin enables input-specific homeostatic plasticity. *EMBO J.* **41**, e109012 (2022).
51. Sun, Z. et al. Mass spectrometry analysis of newly emerging coronavirus HCoV-19 spike protein and human ACE2 reveals camouflaging glycans and unique post-translational modifications. *Engineering* **7**, 1441–1451 (2021).
52. Lorenzo, R. et al. Deamidation drives molecular aging of the SARS-CoV-2 spike protein receptor-binding motif. *J. Biol. Chem.* **297**, 101175 (2021).
53. Zhao, J., Li, J., Xu, S. & Feng, P. Emerging roles of protein deamidation in innate immune signaling. *J. Virol.* **90**, 4262–4268 (2016).
54. Arcos-Burgos, M. et al. A common variant of the latrophilin 3 gene, LPHN3, confers susceptibility to ADHD and predicts effectiveness of stimulant medication. *Mol. Psychiatry* **15**, 1053–1066 (2010).
55. Lange, M. et al. The ADHD-susceptibility gene lphn3.1 modulates dopaminergic neuron formation and locomotor activity during zebrafish development. *Mol. Psychiatry* **17**, 946–954 (2012).
56. Regan, S. L. et al. A novel role for the ADHD risk gene latrophilin-3 in learning and memory in Lphn3 knockout rats. *Neurobiol. Dis.* **158**, 105456 (2021).
57. Domene, S. et al. Screening of human LPHN3 for variants with a potential impact on ADHD susceptibility. *Am. J. Med. Genet. B* **156B**, 11–18 (2011).
58. Orsini, C. A. et al. Behavioral and transcriptomic profiling of mice null for Lphn3, a gene implicated in ADHD and addiction. *Mol. Genet. Genomic Med.* **4**, 322–343 (2016).
59. Wallis, D. et al. Initial characterization of mice null for Lphn3, a gene implicated in ADHD and addiction. *Brain Res.* **1463**, 85–92 (2012).

60. Li, J. et al. Alternative splicing controls teneurin-latrophilin interaction and synapse specificity by a shape-shifting mechanism. *Nat. Commun.* **11**, 2140 (2020).
61. Giandomenico, S. L. et al. Cerebral organoids at the air–liquid interface generate diverse nerve tracts with functional output. *Nat. Neurosci.* **22**, 669–679 (2019).
62. Trujillo, C. A. et al. Complex oscillatory waves emerging from cortical organoids model early human brain network development. *Cell Stem Cell* **25**, 558–569 e557 (2019).
63. Chaumont, H. et al. Long-term outcomes after NeuroCOVID: a 6-month follow-up study on 60 patients. *Rev. Neurol.* **178**, 137–143 (2022).
64. Coulter, M. E. et al. The ESCRT-III protein CHMP1A mediates secretion of sonic hedgehog on a distinctive subtype of extracellular vesicles. *Cell Rep.* **24**, 973–986 e978 (2018).
65. Gee, G. V., Manley, K. & Atwood, W. J. Derivation of a JC virus-resistant human glial cell line: implications for the identification of host cell factors that determine viral tropism. *Virology* **314**, 101–109 (2003).
66. Rebendenne, A. et al. SARS-CoV-2 triggers an MDA-5-dependent interferon response which is unable to control replication in lung epithelial cells. *J. Virol.* **95**, e02415–e02420 (2021).
67. Bouyssie, D. et al. Proline: an efficient and user-friendly software suite for large-scale proteomics. *Bioinformatics* **36**, 3148–3155 (2020).
68. Wieczorek, S., Combes, F., Borges, H. & Burger, T. Protein-level statistical analysis of quantitative label-free proteomics data with ProStaR. *Methods Mol. Biol.* **1959**, 225–246 (2019).
69. Hulstaert, N. et al. ThermoRawFileParser: modular, scalable, and cross-platform RAW file conversion. *J. Proteome Res.* **19**, 537–542 (2020).
70. Degroeve, S., et al. ionbot: a novel, innovative and sensitive machine learning approach to LC-MS/MS peptide identification. Preprint at *bioRxiv* https://doi.org/10.1101/2021.07.02.450686 (2021).
71. Lutz, W. WillyLutz/electrical-analysis-sars-cov-2. *GitHub* https://github.com/WillyLutz/electrical-analysis-sars-cov-2 (2024).
72. Perez-Riverol, Y. et al. The PRIDE database resources in 2022: a hub for mass spectrometry-based proteomics evidences. *Nucleic Acids Res.* **50**, D543–D552 (2022).

Acknowledgements

Image acquisitions in BSL-2 environment were performed at the MRI imaging facility (CNRS, Univ Montpellier), which also provided advice and training. All infections and live cell imaging using replication-competent SARS-CoV-2 were performed at the Center for the study of infectious diseases and anti-infectious pharmacology (CEMIPAI) BSL-3 facility (CNRS, Univ Montpellier). We acknowledge S. van der Werf (Institut Pasteur) for providing us very early with the wild-type SARS-CoV-2 strains. We also acknowledge the World Reference Center for Emerging Viruses and Arboviruses and University of Texas Medical Branch (UTMB) investigator P. Y. Shi for providing the SARS-CoV-2 mNeonGreen and NanoLuc reporter viruses. We thank C. Bernou for participating in the preparation of OPAB (IRIM, CNRS), S. Lebrun (IRIM, CNRS) and D. Brychka (IRIM, CNRS) for contributing to cerebral organoid production for the revision stage of this article, and all the members of the Gaudin Lab for helpful discussions.

Funders: CNRS INSB (R.G.), Agence Nationale de la Recherche ANR-20-CE15-0019-01 (R.G.), Agence Nationale de la Recherche ANR-21-CE33-0007-03 (R.G., S.C. and G.G.), Agence Nationale de la Recherche ANR-22-CE15-0007-01 (R.G.), Health, Biology and Chemical Sciences (CBS2) Montpellier doctoral school (E.P.), Agence Nationale de la Recherche ANR-10-INBS-08-03; Proteomics French Infrastructure (ProFI) FR2048 (C.C.), Isite MUSE (Montpellier University of Excellence) (B.C.), European Union's Horizon 2020 Programme (H2020-INFRAIA-2018-1) (823839) (L.M.), Research Foundation Flanders (FWO) (G028821N) (L.M.), Research Foundation Flanders (FWO) (1S57123N) (T.C.), Ghent University Concerted Research Action (BOF21/GOA/033) (L.M.), Fondation pour la Recherche Médicale, MIE202207016212 (E.P., R.G.), Fondation pour la Recherche Médicale, SPF202110014043 (Y.B.), Labex NUMEV–SATIS Project (B.G.). The funders had no role in the study design, data collection and analysis, decision to publish or preparation of the manuscript.

Author contributions

Conceptualization: E.P. and R.G. Methodology: E.P., A.H., W.L., T.C., F.D., M.S.D., Y.B., J.R.E.R., B.G., J.B., L.M., F.M.J.J., B.C., C.C., S.C., G.G. and R.G. Investigation: E.P., A.H., F.D., W.L., M.S.D., Y.B., J.R.E.R., J.B., D.C., L.A., M.L., C.C., S.C., G.G. and R.G. Analysis: E.P., A.H., F.D., W.L., T.C., L.M., M.S.D., Y.B., J.B., D.C., L.A., M.L., V.R., C.C., S.C., G.G. and R.G. Supervision: L.M., C.C., S.C., G.G., R.G. Writing—original draft: R.G. Writing—review and editing: E.P., A.H., T.C., L.M., M.S.D., D.C., C.C., S.C., G.G. and R.G.

Competing interests

The authors declare no competing interests.

Additional information

Extended data is available for this paper at https://doi.org/10.1038/s41564-024-01657-2.

Supplementary information The online version contains supplementary material available at https://doi.org/10.1038/s41564-024-01657-2.

Correspondence and requests for materials should be addressed to Raphael Gaudin.

Reviewer Recognition *Nature Microbiology* thanks Patricia Garcez, Harris Gelbard, Kaustubh Patil, Sydney Stein and Jan Zrimec for their contribution to the peer review of this work. Peer reviewer reports are available.

Reprints and permissions information is available at www.nature.com/reprints.

[1]CNRS, Institut de Recherche en Infectiologie de Montpellier (IRIM), Montpellier, France. [2]Univ Montpellier, Montpellier, France. [3]Laboratoire de Spectrométrie de Masse Bio-Organique, IPHC, UMR 7178, CNRS-Université de Strasbourg, Strasbourg, France. [4]Infrastructure Nationale de Protéomique ProFI—FR2048, Strasbourg, France. [5]EDPFM (Equipe de Droit Pénal et de Sciences Forensiques de Montpellier), Univ Montpellier, Montpellier, France. [6]Emergency Pole, Forensic Medicine Department, Montpellier University Hospital, Montpellier, France. [7]UM-CNRS Laboratoire d'Informatique de Robotique et de Microelectronique de Montpellier (LIRMM), Montpellier, France. [8]VIB-UGent Center for Medical Biotechnology, VIB, Ghent, Belgium. [9]Department of Biomolecular Medicine, Ghent University, Ghent, Belgium. [10]Swammerdam Institute for Life Sciences, University of Amsterdam, Amsterdam, The Netherlands. [11]University of Reims Champagne-Ardenne, Medicine Faculty, Laboratory of Virology, CardioVir UMR-S 1320, Reims, France. [12]Forensic, Virology and ENT Departments, University Hospital Centre (CHU), Reims, France. [13]Anatomy laboratory, UFR Médecine, Université de Reims Champagne-Ardenne, Reims, France. [14]Pathological Department and Biological Resources Center BRC, Montpellier University Hospital, 'Cerebral plasticity, Stem cells and Glial tumors' team. IGF- Institut de génomique fonctionnelle INSERM U 1191 - CNRS UMR 5203, Univ Montpellier, Montpellier, France. [15]Institut d'Electronique et des Systèmes (IES), CNRS, Montpellier, France. ✉e-mail: raphael.gaudin@irim.cnrs.fr

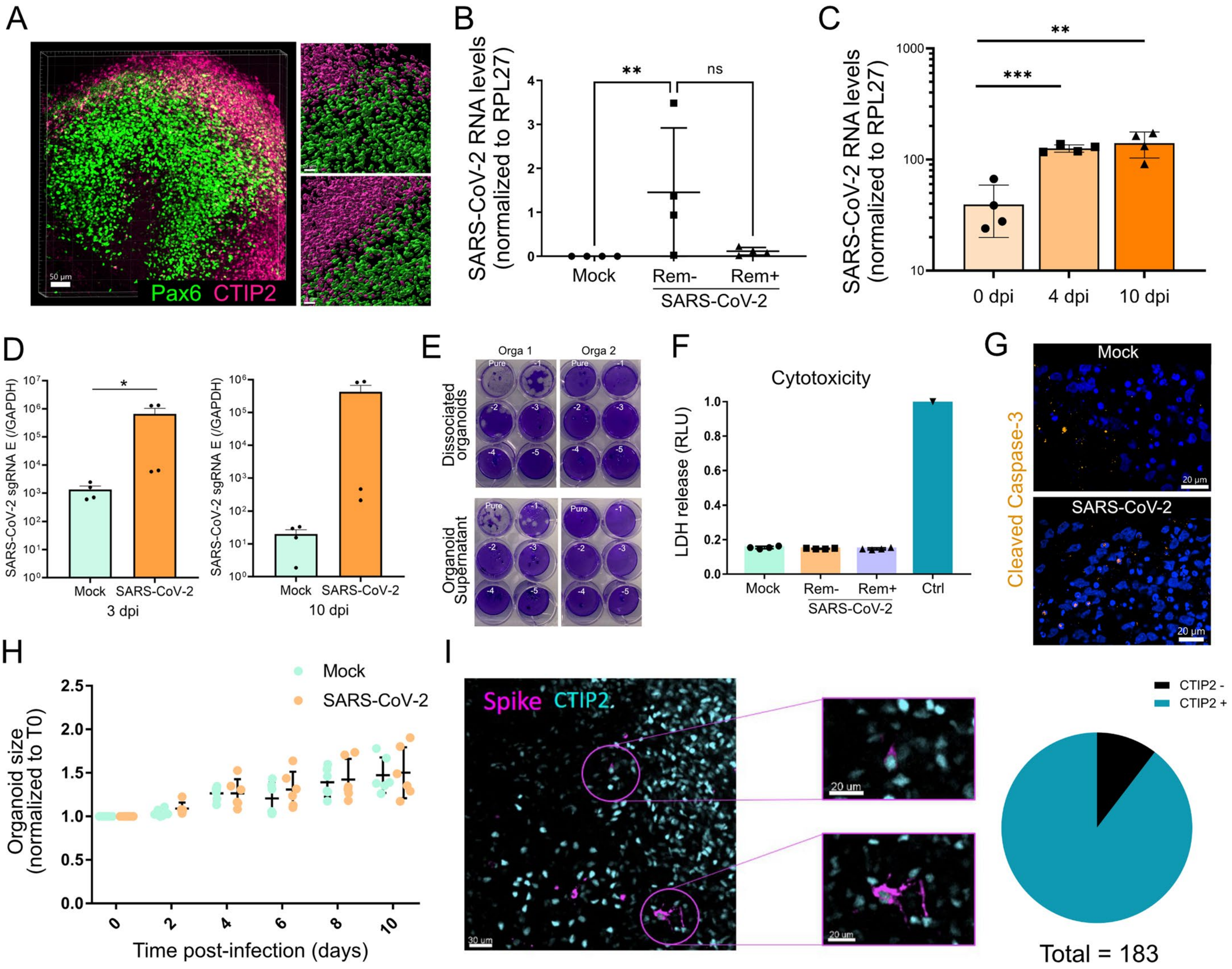

Extended Data Fig. 1 | Characterization of SARS-CoV-2-exposed cerebral organoids. (**a**) Three-dimensional imaging of a cerebral organoid differentiated for 45 days stained for neural progenitor (Pax6, green), and neurons (CTIP2, purple). (**b**–**d**) Cerebral organoids differentiated for 45 days were mock-infected or infected for 10 days (B) or at indicated time (C-D) with SARS-CoV-2 at 105 pfu/organoid in the presence or absence of 10 µM Remdesivir. RNA extraction and RT-qPCR were performed and the data corresponds to SARS-CoV-2 RNA levels using the N1 primers and normalized by RPL27 (C) from n of 2 organoids per condition in duplicates or to SARS-CoV-2 RNA levels using the sgRNA E primers and normalized by GAPDH (D) from n of 2 organoids per condition in duplicates. Data are presented as mean values +/− SD (C) or +/− SEM (D). (C) Two-tailed p value (Kruskal-Wallis test) was 0.0045 (**) or 0.3268 (ns). (D) Two-tailed p value from paired t test was< 0.0385 (*). (**e**–**i**) Cerebral organoids differentiated for 45 days were mock-infected or infected for 10 days with SARS-CoV-2 at 105 pfu/organoid. (E) The organoid supernatant or dissociated organoids were used for titration by plaque assay on Vero E6 cells. The labels pure to -6 correspond to log10 dilution factors. (**f**) LDH release was measured in the supernatant of the organoids. The data are from a n of two organoids per condition in duplicates and shows no toxicity in any condition, except for Ctrl, a positive control used to account for maximum cytotoxicity. Data are presented as mean values +/− SD. (**g**) Cerebral organoids were fixed, permeabilized and stained with the anti-cleaved Caspase 3 antibody (orange, a cell death marker, and Dapi (blue). The micrographs show marginal apoptotic staining in both conditions. (**h**) The organoid size was measured every 2 days for 10 days. Data are presented as mean values +/− SD and each dot corresponds to single organoids with n = 6 organoid per time point. No significant difference in size was found between mock and SARS-CoV-2 infected organoids over time. (**i**) Cerebral organoids differentiated for 45 days were and stain for Spike and the neuronal marker CTIP2. The micrograph and insets show CTIP2-positive infected cells. The pie chart made from 3 fields of view shows that ≈ 90% of the infected cells were positive for CTIP2.

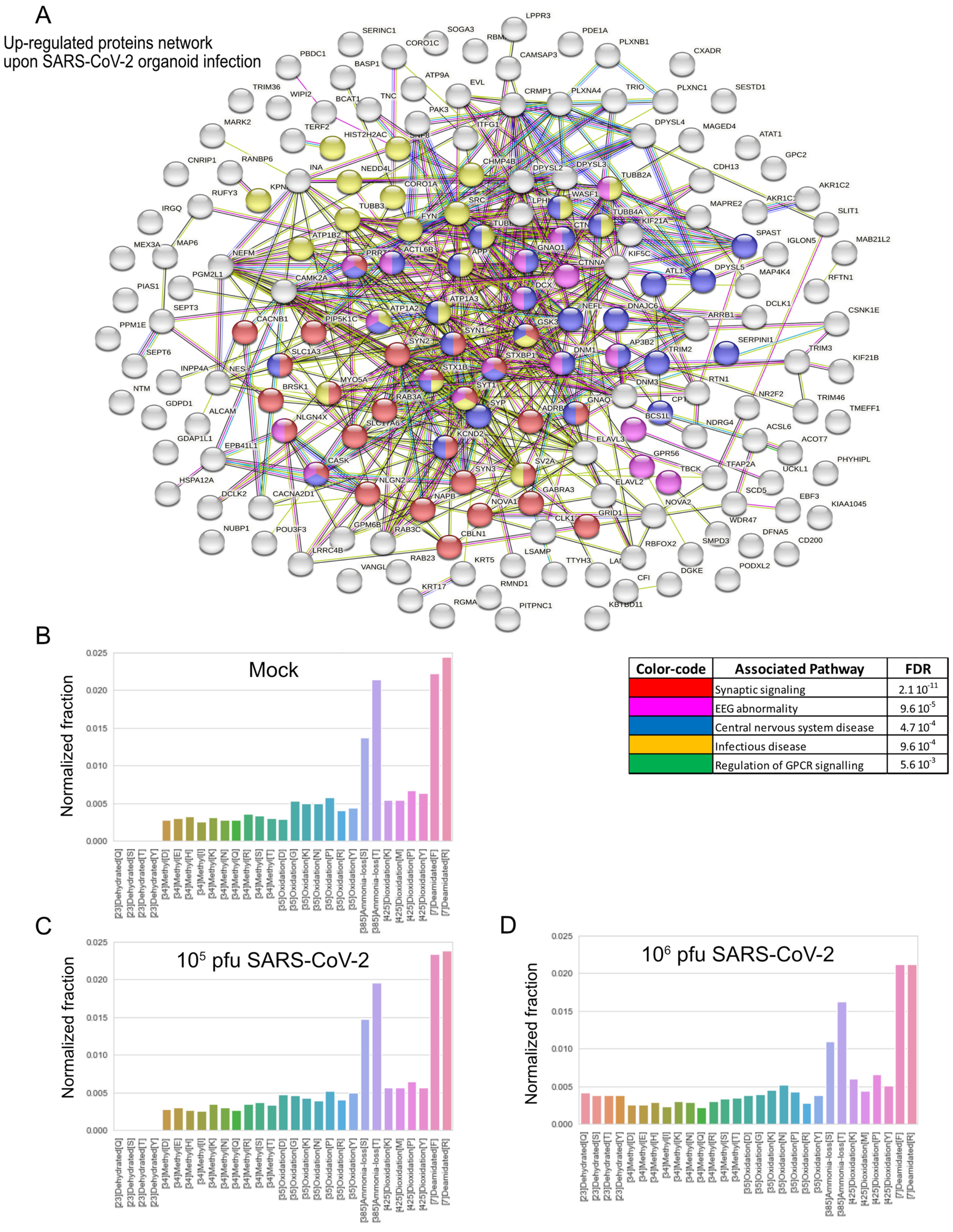

Color-code	Associated Pathway	FDR
🟥	Synaptic signaling	$2.1\ 10^{-11}$
🟪	EEG abnormality	$9.6\ 10^{-5}$
🟦	Central nervous system disease	$4.7\ 10^{-4}$
🟨	Infectious disease	$9.6\ 10^{-4}$
🟩	Regulation of GPCR signalling	$5.6\ 10^{-3}$

Extended Data Fig. 2 | See next page for caption.

Extended Data Fig. 2 | Single-organoid proteomic analysis (associated to Supplementary Table 1 and 2). Cerebral organoids differentiated for 45 days were mock-infected or infected for 10 days with SARS-CoV-2 at 10^5 pfu or 10^6 pfu per organoid and processed for single-organoid differential proteomics comparing infected organoids to their non-infected counterparts using nanoLC-MS/MS. (**a**) Protein network analysis using GSEA of the upregulated cellular component upon infection of cerebral organoids. (**b**–**e**) Patterns of differential post-translational modifications (PTM) in mock-infected (**B**), and SARS-CoV-2-infected samples at 10^5 pfu (**C**) or 10^6 pfu (**D**) were obtained by averaging relative quantifications.

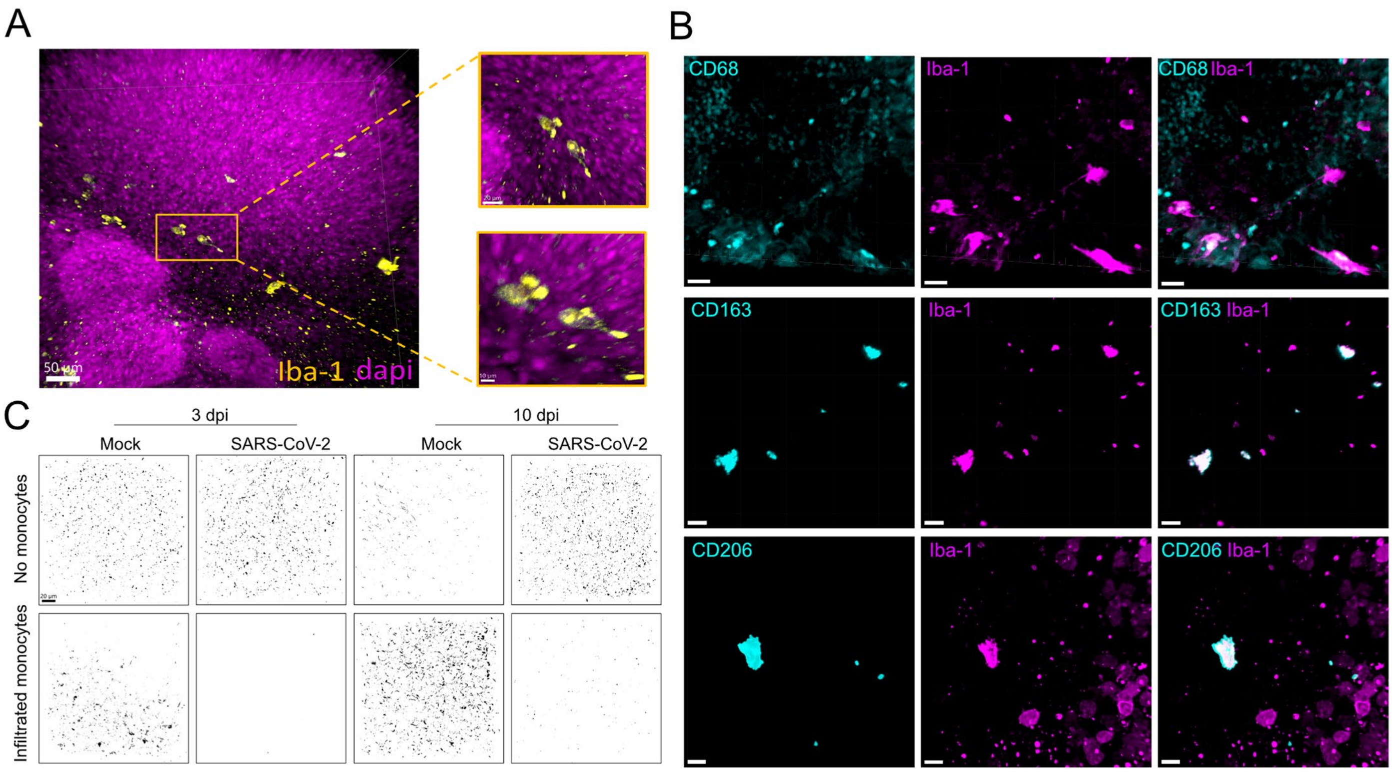

Extended Data Fig. 3 | SARS-CoV-2 infection of cerebral organoids containing infiltrated monocytes. (**a**) Cerebral organoids differentiated for 45 days were cocultured for 7 days with human primary monocytes and stained for Iba-1 (orange) and Dapi (purple). The micrograph is representative of fields of views originating from 2 organoids. (**b**) Cerebral organoids differentiated for 45 days were cocultured for 7 days with human primary monocytes and Mock infected for 10 days. The organoids were stained for CD68, CD163 or CD206 (cyan) and Iba-1 (purple). Each staining panel represents one organoid. (**c**) Cerebral organoids differentiated for 45 days were cocultured for 7 days in the absence or presence of human primary monocytes, infected for 3 or 10 days with SARS-CoV-2 at 105 pfu and stained for Bassoon.

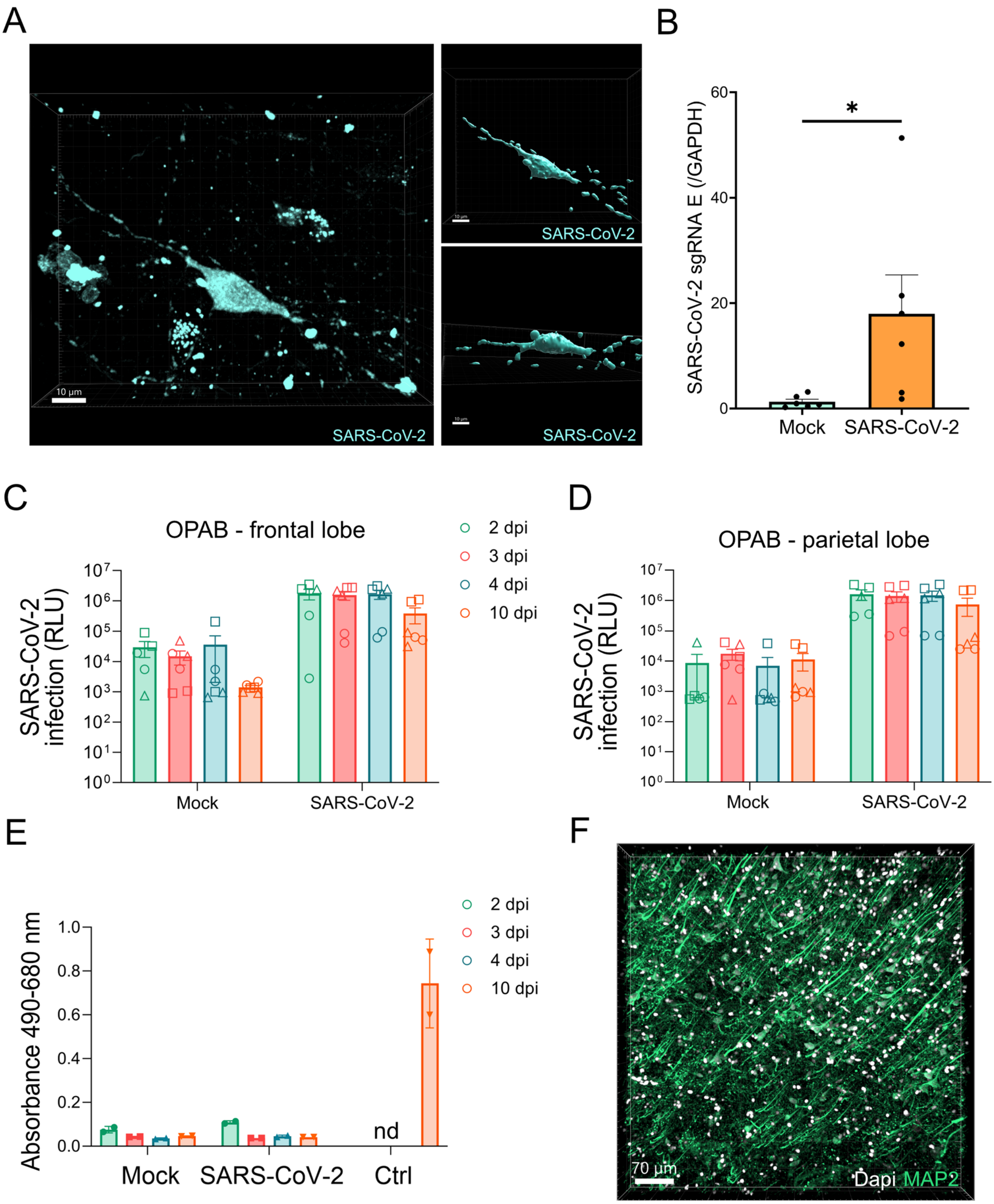

Extended Data Fig. 4 | SARS-CoV-2 infection of human post mortem brain slices. OPAB were mock-infected or infected with SARS-CoV-2 at 105 pfu/well. (**a**) Three-dimensional snapshots of a slice infected with a replication-competent SARS-CoV-2 mNeonGreen reporter virus. (**b**) RNA extraction and RT-qPCR were performed and the data corresponds to SARS-CoV-2 sgRNA levels normalized by GAPDH housekeeping gene from n of 3 OPAB from 2 donors. Data are presented as mean values +/− SEM. Two-tailed p value from unpaired t test was 0.0483 (*). (**c-d**) Infection kinetics of OPAB derived from the frontal lobe (C) and parietal lobe (D) using a replication-competent SARS-CoV-2 NanoLuciferase (NLuc) reporter virus. Each dot corresponds to a single slice and the symbols discriminate between the donors. Data are presented as mean values +/− SD, with n of 2 OPAB from 3 donors. (**e**) Cytotoxicity is measured for each condition from the parietal lobe from one donor using an LDH release luminescence assay. Data are presented as mean values +/− SD. nd: not determined. (**f**) Three-dimensional imaging of neurons (MAP2) from human brain slices exposed to SARS-CoV-2. The neurons from SARS-CoV-2-exposed brain slices retain densely aligned organization.

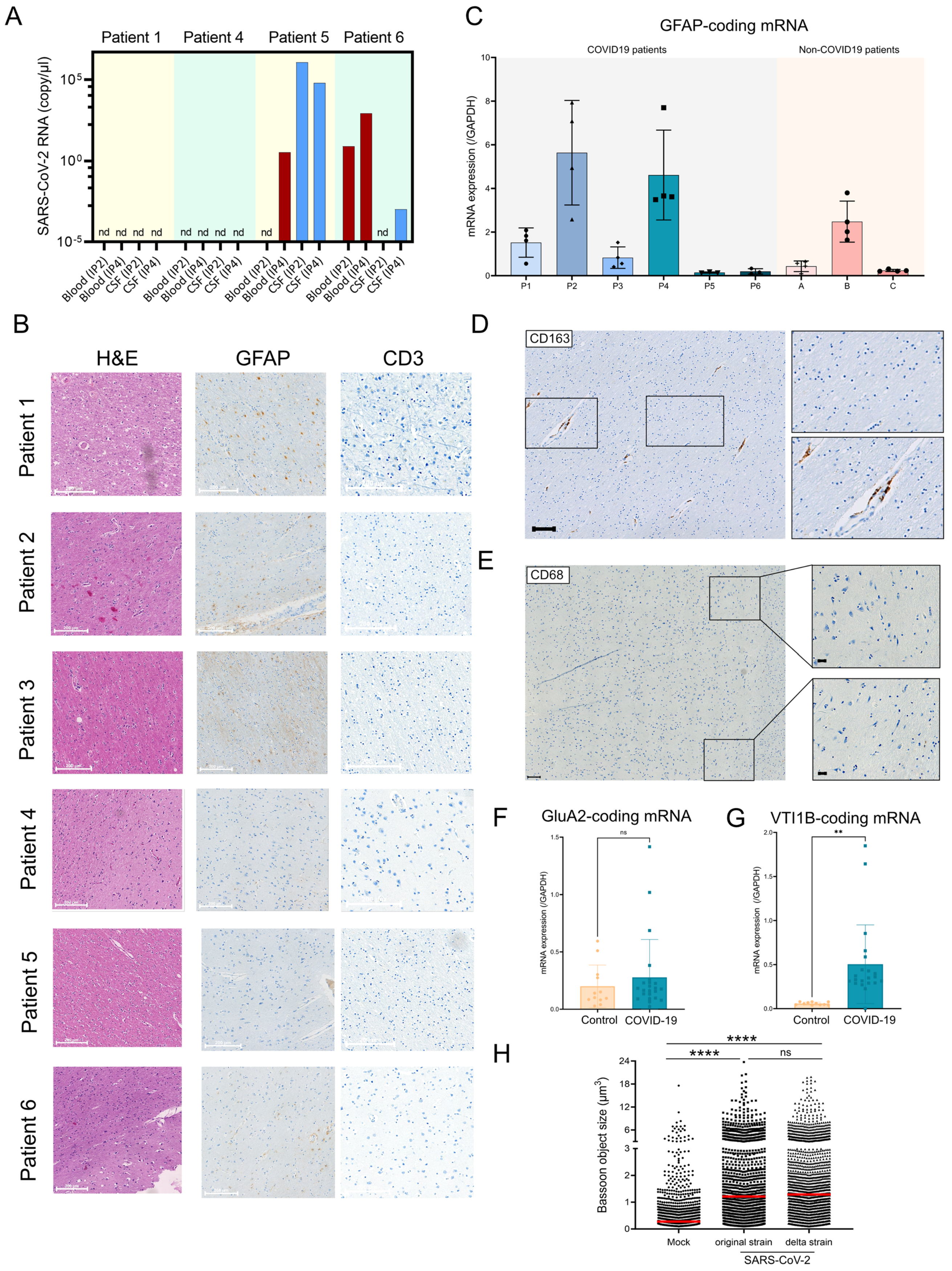

Extended Data Fig. 5 | See next page for caption.

Extended Data Fig. 5 | Characterization of the brain features of COVID-19 patients without neurological symptoms. (**a**) RT-qPCR of the blood and cerebrospinal fluid (CSF) of 4 COVID-19 patients using two anti SARS-CoV-2 probe sets (IP2 and IP4). GAPDH was also acquired. Color coding shows blood in red and CSF in blue. ND: not determined. (**b**) Imaging of Hematoxylin and Eosin (H&E), GFAP and CD3 stainings of the frontal lobe of 6 COVID-19 patients using 10X magnification. (**c**) RT-qPCR from temporal lobe of 6 COVID-19 patient or 3 non-COVID-19 patients were performed in duplicates to evaluate the presence of astrocytes. The graph corresponds to GFAP mRNA expression normalized to GAPDH mRNA. Data are presented as mean values +/− SD. (**d**, **e**) Imaging of CD163 (D) and CD68 (E) staining of the frontal lobe of COVID-19 patients using 10X magnification. Scale bar = 100 µm. (**f-g**) RNA extraction and RT-qPCR from the temporal lobe of COVID-19 or individuals without COVID-19 (control) were performed and the data corresponds to the mRNA levels coding for GluA2 (F), or VTI1B (G) normalized by GAPDH. Each dot corresponds to an individual measurement obtained from at least two individual explants collected from 3 non-COVID-19 (control) and 6 COVID-19 patients in duplicates. Data are presented as mean values +/− SD. Two-tailed p value from unpaired t test was 0.026 (**) or 0.4584 (ns). (**h**) OPAB were mock-infected or infected with the original strain or the delta strain of SARS-CoV-2 at 105 pfu/well. The graph shows the distribution of Bassoon object volumes for each condition. Each dot corresponds to single Bassoon objects obtained from a n of 3 OPAB. Two-tailed p value from unpaired t test was < 0.0001 (****) or 0.1879 (ns).

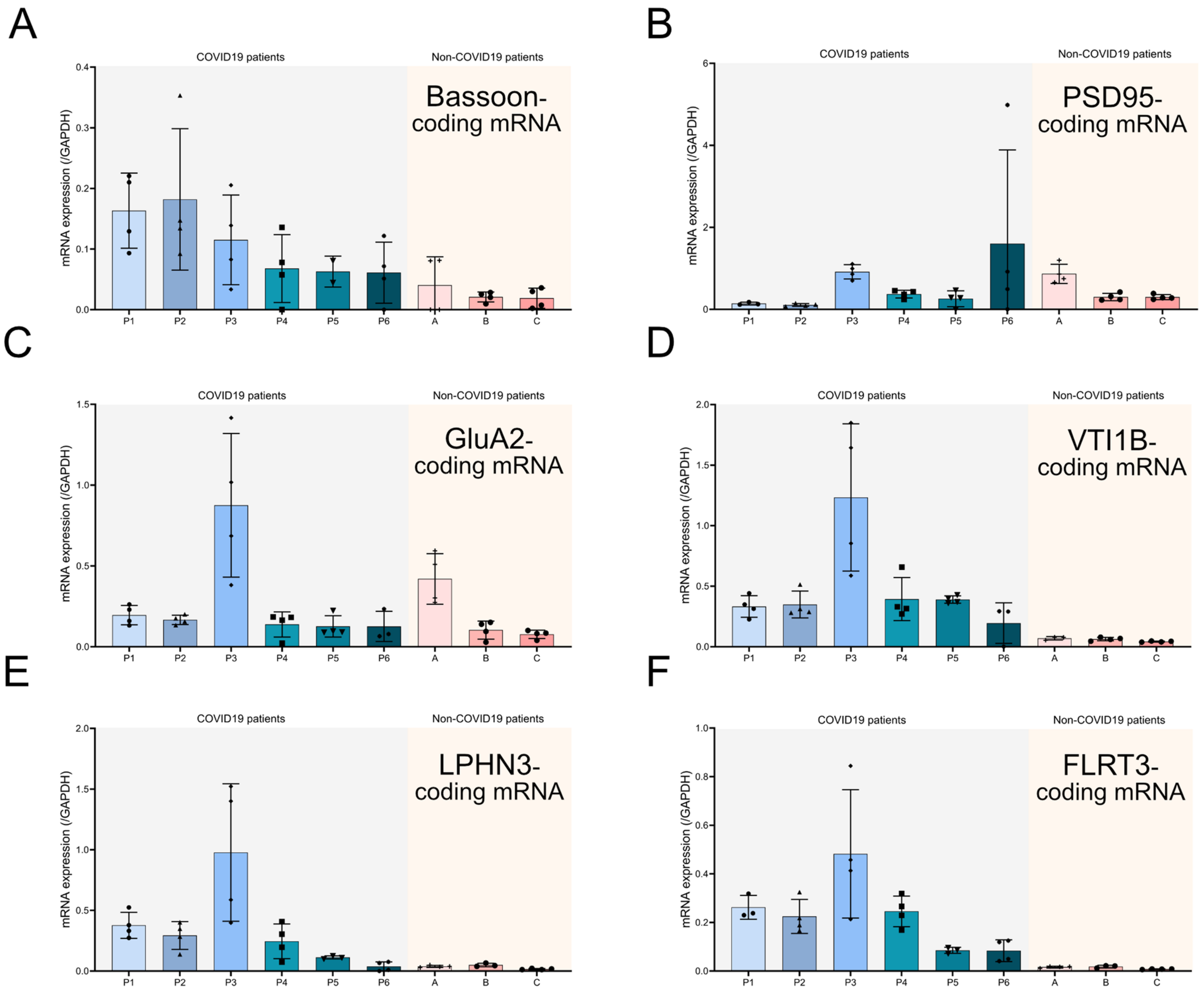

Extended Data Fig. 6 | RNA expression upregulation of synapse-coding genes in COVID-19 patients. RT-qPCR from temporal lobe of 6 COVID-19 patient or 3 non-COVID-19 patient were performed and the data corresponds to the mRNA level normalized by GAPDH of Bassoon (**a**), PSD95 (**b**), GluA2 (**c**), VTI1B (**d**), LPHN3 (E) and FLRT3 (**f**). Data are presented as mean values +/− SD.

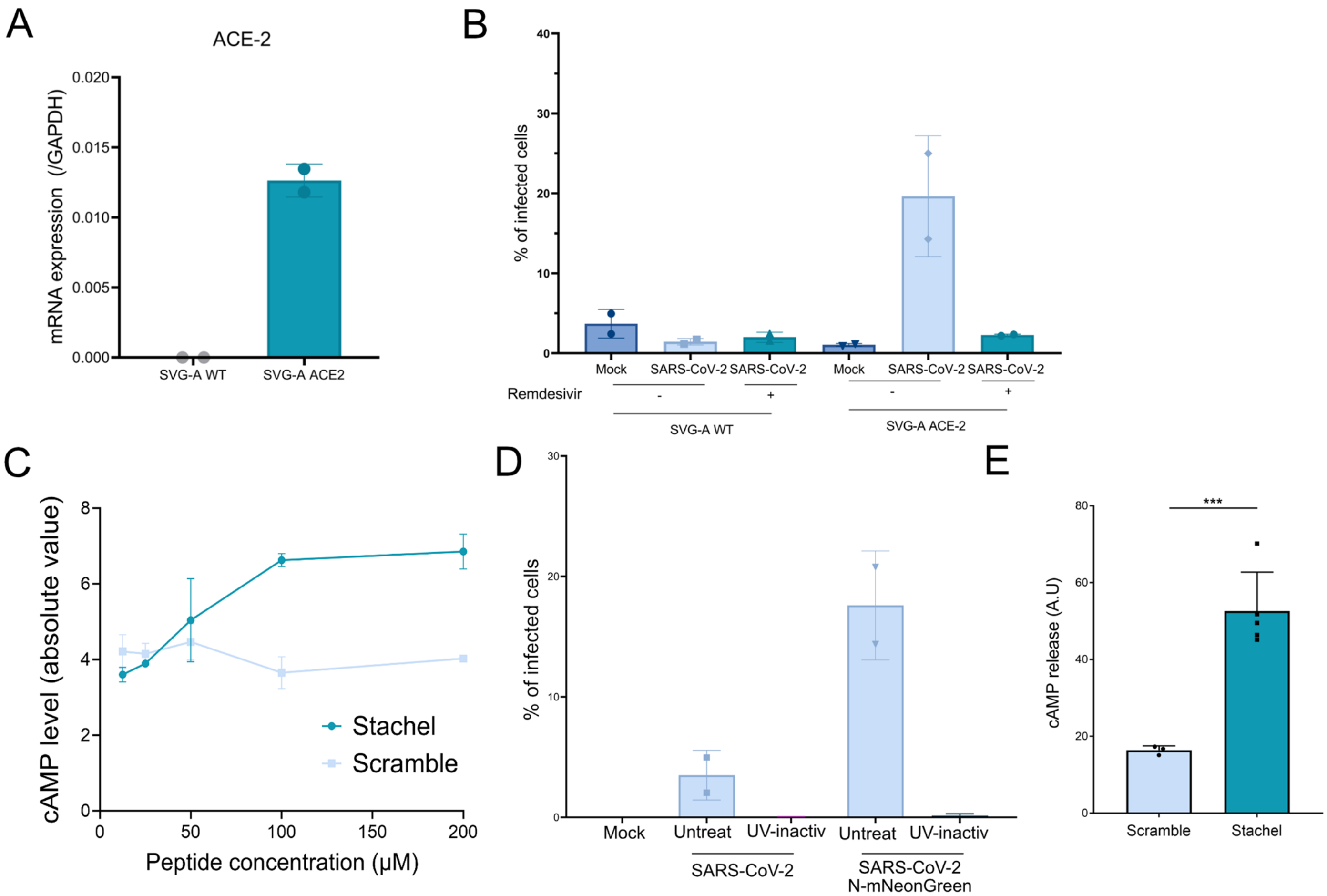

Extended Data Fig. 7 | Characterization of the SVG-A ACE2 cell line. (**a**) RNA extraction and qPCR of ACE-2 mRNA from SVGA stably expressing ACE-2 and normalized to GAPDH mRNA. Data are presented as mean values +/− SD from duplicates from one experiment. (**b**) SVG-A WT and SVG-A ACE-2 infected with SARS-CoV-2 mNeonGreen for 24 hours treated or not with 10µM Remdesivir. The graph represents the percentage of infected cells quantify by flow cytometry. Data are presented as mean values +/− SD from duplicates from one experiment. (**c**) SVG-A were treated with the concentration of Stachel peptide (agonist) or Scramble peptide (control) as indicated. The graph represents the amount of cAMP released after LPHN3 stimulation. Data are presented as mean values +/− SD from triplicates from one experiment. (**d**) SVGA-ACE2 were infected for 48 h with SARS-CoV-2 WT or SARS-CoV-2 N-mNeonGreen inactivated or not with UV-C (254 nm) as indicated. Cells were stained with Spike for Flow cytometry analysis. The bar graph represents the percentage of infected cells in each condition. Data are presented as mean values +/− SD from duplicates from one experiment. (**e**) Cerebral organoids were treated with Scramble or Stachel peptides. The graph represents the cAMP released after LPHN3 stimulation. Data are presented as mean values +/− SD from triplicates from one experiment. Two-tailed p value from unpaired t test was 0.001 (***).

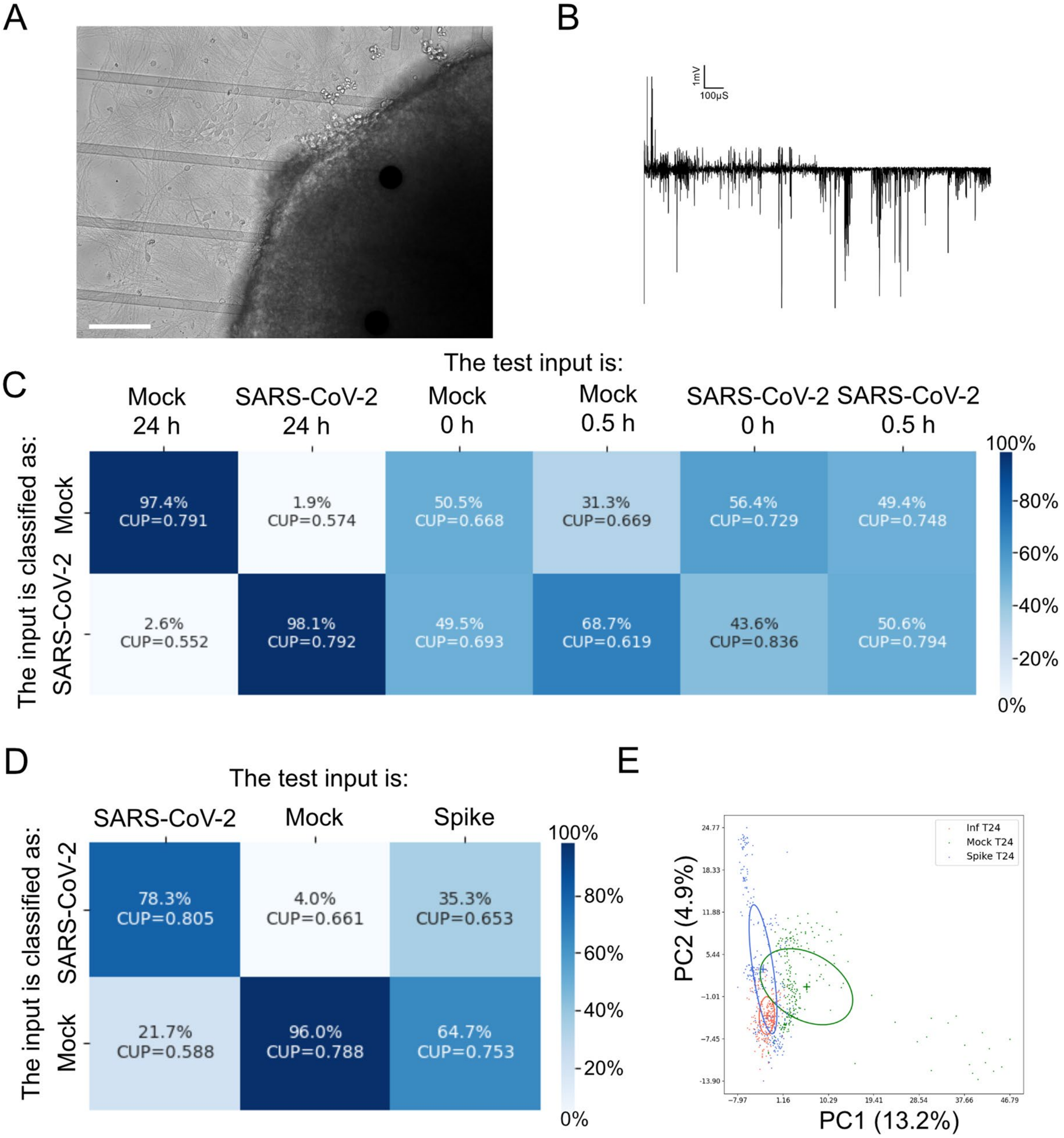

Extended Data Fig. 8 | Impact of SARS-CoV-2 exposure on organoid electrical activity. (**a**) Micrograph of an organoid on a 3D MEA electrode, representative of at least ten organoids. Scale bar = 30 µm. (**b**) Extracellular electrical trace of an electrode on which a SARS-CoV-2-exposed cerebral organoid was seeded. (**c**) Confusion matrix for time-wise testing. The model has been trained on recordings of infected and mock condition 24 hpi, and tested on 0 hpi, 0.5 hpi and 24 hpi for SARS-CoV-2 infected and mock conditions. CUP: Confidence Upon Prediction. (**d**) Confusion matrix for testing the impact of Spike. The rows represent the different outputs the RFC model has been trained to recognize. The columns represent the data we provided to the model for testing purposes. The model has been trained on recordings of infected and mock condition at 24 hpi, and tested on recordings of infected, mock, and Spike-treated infected condition at 24 hpi. CUP: Confidence Upon Prediction. (E) Principal component analysis fitted on mock and infected conditions at 24 hpi, then applied on the Spike-treated infected recordings 24 hpi. The ellipses represent the confidence for each condition.

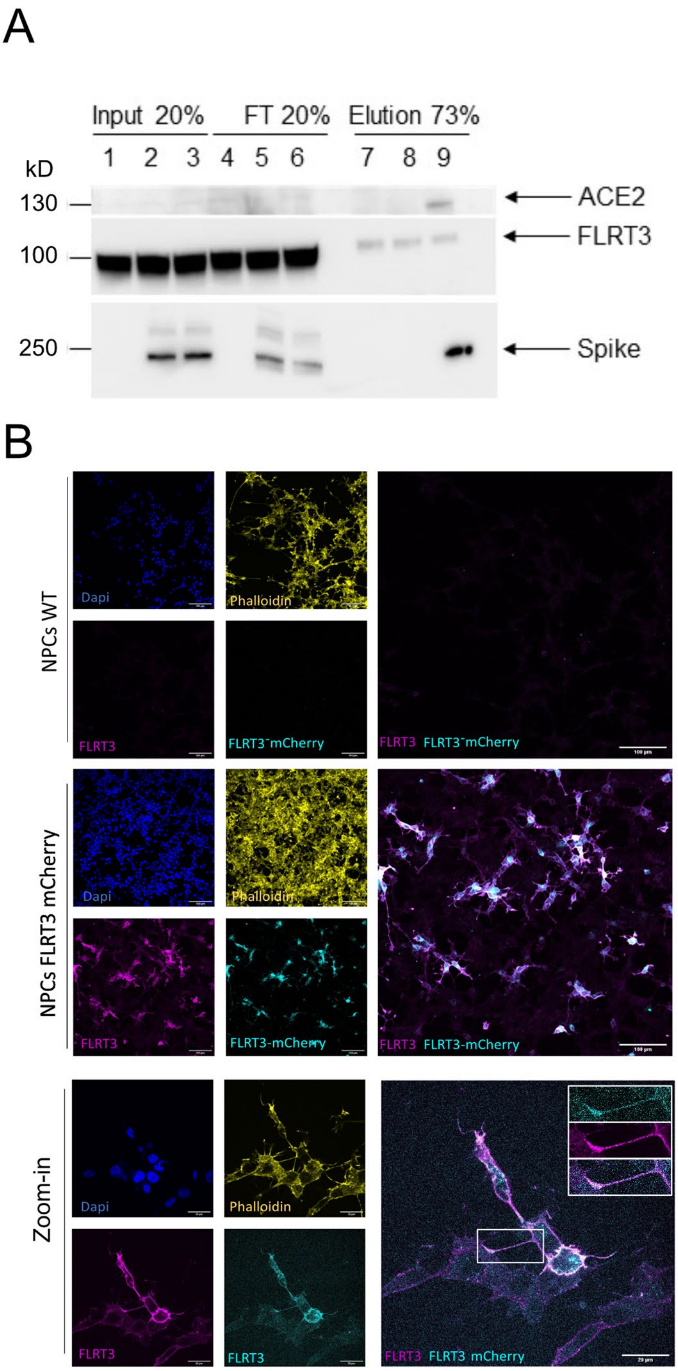

Extended Data Fig. 9 | Characterization of human neural progenitor cells. (**a**) Mature neurons derived from hNPCs were incubated with recombinant Spike protein for 3 h and immunoprecipitation of Spike was performed using protein A-coupled agarose beads. Western blotting for ACE2, FLRT3 and Spike shows that pull-down of the Spike protein was efficient, and that neuronal ACE2 could be retrieved associated to Spike, while undetectable from the input. However, no FLRT3 could be enriched upon Spike pull-down using this method. The western blot is representative of two experiments. (**b**) NPCs were transduced with FLRT3 mCherry construct. The micrograph (left panel) and zoom-in (right panel) shows NPCs expressing fluorescent FLRT3 and positive for FLRT3 staining. The micrograph is representative at least 15 fields of view.

nature portfolio

Corresponding author(s): Gaudin
Last updated by author(s): Feb 20, 2024

Reporting Summary

Nature Portfolio wishes to improve the reproducibility of the work that we publish. This form provides structure for consistency and transparency in reporting. For further information on Nature Portfolio policies, see our Editorial Policies and the Editorial Policy Checklist.

Statistics

For all statistical analyses, confirm that the following items are present in the figure legend, table legend, main text, or Methods section.

n/a	Confirmed	
☐	☒	The exact sample size (*n*) for each experimental group/condition, given as a discrete number and unit of measurement
☐	☒	A statement on whether measurements were taken from distinct samples or whether the same sample was measured repeatedly
☐	☒	The statistical test(s) used AND whether they are one- or two-sided *Only common tests should be described solely by name; describe more complex techniques in the Methods section.*
☒	☐	A description of all covariates tested
☐	☒	A description of any assumptions or corrections, such as tests of normality and adjustment for multiple comparisons
☐	☒	A full description of the statistical parameters including central tendency (e.g. means) or other basic estimates (e.g. regression coefficient) AND variation (e.g. standard deviation) or associated estimates of uncertainty (e.g. confidence intervals)
☐	☒	For null hypothesis testing, the test statistic (e.g. *F*, *t*, *r*) with confidence intervals, effect sizes, degrees of freedom and *P* value noted *Give P values as exact values whenever suitable.*
☒	☐	For Bayesian analysis, information on the choice of priors and Markov chain Monte Carlo settings
☐	☒	For hierarchical and complex designs, identification of the appropriate level for tests and full reporting of outcomes
☒	☐	Estimates of effect sizes (e.g. Cohen's *d*, Pearson's *r*), indicating how they were calculated

Our web collection on statistics for biologists contains articles on many of the points above.

Software and code

Policy information about availability of computer code

Data collection	AxioObserver.Z1 inverted microscope (Zeiss) mounted with a spinning disc head (Yokogawa), a back-illuminated EMCCD camera (Evolve; Photometrics) spinning-disk confocal microscope (Dragonfly, Oxford Instruments) equipped with an ultrasensitive 1024×1024 EMCCD camera (iXon Life 888, Andor) and four laser lines (405, 488, 561, and 637nm) nanoAcquity UltraPerformance Liquid Chromatography device (Waters Corporation) coupled to a quadrupole-Orbitrap mass spectrometer (Q-Exactive HF-X, Thermo Fisher Scientific) PELCO easislicer (Ted Pella) PerkinElmer EnVision spectro-luminometer Autostainer BenchMark ULTRA (Ventana Medical Systems) ChemiDoc imaging system (Bio-Rad) iBlot2 (ThermoFisher) ionbot search engine (v0.7.0) MEA2100-Mini headstage (MultiChannel System)

Data analysis	Bitplane Imaris x64 (Oxford Instruments) version 9.2 and 9.7 FiJi (ImageJ) GraphPad Prism version 9 ProStaR software Matlab R2022a Microsoft Excel 2019

For manuscripts utilizing custom algorithms or software that are central to the research but not yet described in published literature, software must be made available to editors and reviewers. We strongly encourage code deposition in a community repository (e.g. GitHub). See the Nature Portfolio guidelines for submitting code & software for further information.

Data

Policy information about availability of data

All manuscripts must include a data availability statement. This statement should provide the following information, where applicable:

- Accession codes, unique identifiers, or web links for publicly available datasets
- A description of any restrictions on data availability
- For clinical datasets or third party data, please ensure that the statement adheres to our policy

All data are available in the main text, extended data and supplementary materials. The plasmid coding for N-mNeonGreen or N-mRuby3 from SARS-CoV-2 is available on Addgene (#170467 and #170466 respectively). The mass spectrometry proteomic data have been deposited to the ProteomeXchange Consortium via the PRIDE partner repository with the dataset identifier PXD036485.

Human research participants

Policy information about studies involving human research participants and Sex and Gender in Research.

Reporting on sex and gender	Sex and gender were not considered in this study.
Population characteristics	All the data presented for organotypic culture of brain explant originate from 4 patients aged from 25 and 72 years old. The post-mortem samples from COVID-19 patients were obtained from 6 patients with a median age of 64.5-year-old (44 to 79-year-old).
Recruitment	Cadavers were chosen based on the absence of cerebral injury or trauma and the post-mortem interval (PMI) was not exceeding 12 h.
Ethics oversight	institutional review board (IRB) of the CHU of Montpellier and French Biomedicine Agency. Family consent was obtained, and absence of opposition from the patient was checked at the French Biomedicine Agency for each patient.

Note that full information on the approval of the study protocol must also be provided in the manuscript.

Field-specific reporting

Please select the one below that is the best fit for your research. If you are not sure, read the appropriate sections before making your selection.

☒ Life sciences ☐ Behavioural & social sciences ☐ Ecological, evolutionary & environmental sciences

For a reference copy of the document with all sections, see nature.com/documents/nr-reporting-summary-flat.pdf

Life sciences study design

All studies must disclose on these points even when the disclosure is negative.

Sample size	No statistical method was used to predetermine sample size.
Data exclusions	No data were excluded from the analyses.
Replication	Number of replicates for each experiments are indicated in the figure legends.
Randomization	The experiments were not randomized.
Blinding	The investigators were not blinded to allocation during experiments and outcome assessment.

Reporting for specific materials, systems and methods

We require information from authors about some types of materials, experimental systems and methods used in many studies. Here, indicate whether each material, system or method listed is relevant to your study. If you are not sure if a list item applies to your research, read the appropriate section before selecting a response.

Materials & experimental systems

n/a	Involved in the study	
☐	☒	Antibodies
☐	☒	Eukaryotic cell lines
☒	☐	Palaeontology and archaeology
☒	☐	Animals and other organisms
☒	☐	Clinical data
☒	☐	Dual use research of concern

Methods

n/a	Involved in the study	
☒	☐	ChIP-seq
☒	☐	Flow cytometry
☒	☐	MRI-based neuroimaging

Antibodies

Antibodies used	The following antibodies were used for immunofluorescence in this study: rabbit polyclonal anti-MAP2 (1/100, GeneTex), rat monoclonal anti-CTIP2 [25B6] (1/100, BioLegend), rabbit polyclonal anti-Pax6 (1/100, BioLegend), goat polyclonal anti-GFAP (1/100, Novus Biological), rabbit polyclonal anti-Iba1 (1/100, Genetex), mouse monoclonal anti-Spike SARS-CoV-2 [1A9] (1/100, Genetex), mouse monoclonal anti-Bassoon [SAP7F407] (1/50, Enzo Life Sciences), rabbit polyclonal anti-Homer1 (1/50, Synaptic system), rabbit polyclonal anti-LPHN3 (1/100, Proteintech), rabbit polyclonal anti-LPHN3 (1/100, ThermoFisher), goat polyclonal anti-FLRT3 (1/50, R&D Systems), rabbit monoclonal anti-Cleaved Caspase 3 [5A1E] (1/100, Cell Signalling Technologies), mouse monoclonal anti-CD68 [Y1/82A] (1/50, BioLegend), mouse monoclonal anti-CD163 [GHI/61] (1/50, BioLegend), mouse monoclonal anti-CD206 [15-2] (1/50, BioLegend). The following antibodies were used for histology examination: mouse monoclonal anti-NeuroF [2F11](1/100, DAKO), mouse monoclonal anti-NeuN [A60] (1/400, Millipore), rabbit monoclonal anti-Oligo2 [EP112] (1/100, BioSB/diagomics), mouse monoclonal anti-GFAP [6F2] (1/400, DAKO), rabbit anti-CD3 [2GV6] (1/100, Roche), rabbit anti-Spike S1 SARS-CoV-2 [ARC2373] (1/100, Diagomics), mouse anti-Nucleocapsid SARS-CoV-2 [BSB-134] (1/750, Diagomics). The following antibodies were used for immunoblotting in this study: rabbit monoclonal anti-ACE-2 [SN0754] (1/1000, Novus Biological), rabbit polyclonal anti-Actin (1/1000, Genetex), rabbit monoclonal anti-N SARS-CoV-2 [#019] (1/1000, Sino Biological), mouse monoclonal anti-LPHN3 [B-6] (1/500, Santa Cruz Biolotechnology). The following dyes were used in this study: Dapi Nuclear Counterstain (Pierce), Hematoxylin and eosin (H&E), Live/Dead Viability/Cytotoxicity (ThermoFisher), SynaptoRed C2 (Biotium).
Validation	All antibodies are commercially available . Please check validation statements on the manufacturer's website, and/or relevant citations.

Eukaryotic cell lines

Policy information about cell lines and Sex and Gender in Research

Cell line source(s)	HEK 293T cells (unknown origin) Vero E6 cells (ECACC) H9 cells (WiCell) hNPCs (Creative Biolabs)
Authentication	The cell lines used were not authenticated
Mycoplasma contamination	All cells were tested negative. A mycoplasma contamination occured during the course of the study, but cells were trashed. The equipments were decontaminated and a fresh batch of uncontaminated cells was thawed.
Commonly misidentified lines (See ICLAC register)	No misidentified cells were used.